

THE SL2S GALAXY-SCALE LENS SAMPLE. III. LENS MODELS, SURFACE PHOTOMETRY AND STELLAR MASSES FOR THE FINAL SAMPLE

ALESSANDRO SONNENFELD^{1*}, RAPHAËL GAVAZZI², SHERRY H. SUYU^{1,3,4}, TOMMASO TREU^{1†}, AND PHILIP J. MARSHALL^{3,5}

Draft version July 19, 2013

ABSTRACT

We present *Hubble Space Telescope* (*HST*) imaging data and CFHT Near IR ground-based images for the final sample of 56 candidate galaxy-scale lenses uncovered in the CFHT Legacy Survey as part of the Strong Lensing in the Legacy Survey (SL2S) project. The new images are used to perform lens modeling, measure surface photometry, and estimate stellar masses of the deflector early-type galaxies. Lens modeling is performed on the *HST* images (or CFHT when *HST* is not available) by fitting the spatially extended light distribution of the lensed features assuming a singular isothermal ellipsoid mass profile and by reconstructing the intrinsic source light distribution on a pixelized grid. Based on the analysis of systematic uncertainties and comparison with inference based on different methods we estimate that our Einstein Radii are accurate to $\sim 3\%$. *HST* imaging provides a much higher success rate in confirming gravitational lenses and measuring their Einstein radii than CFHT imaging does. Lens modeling with ground-based images however, when successful, yields Einstein radius measurements that are competitive with spaced-based images. Information from the lens models is used together with spectroscopic information from the companion paper IV to classify the systems, resulting in a final sample of 39 confirmed (grade-A) lenses and 17 promising candidates (grade-B,C). This represents an increase of half an order of magnitude in sample size with respect to the sample of confirmed lenses studied in papers I and II. The Einstein radii of the confirmed lenses in our sample span the range 5 – 15 kpc and are typically larger than those of other surveys, probing the mass in regions where the dark matter contribution is more important. Stellar masses are in the range $10^{11} - 10^{12} M_{\odot}$, covering the range of massive ETGs. The redshifts of the main deflector span a range $0.3 \leq z_d \leq 0.8$, which nicely complements low-redshift samples like the SLACS and thus provides an excellent sample for the study of the cosmic evolution of the mass distribution of early-type galaxies over the second half of the history of the Universe.

Subject headings: galaxies: fundamental parameters — gravitational lensing —

1. INTRODUCTION

Strong gravitational lensing is a powerful and consolidated technique for measuring the distribution of matter in massive galaxies at cosmological distances. Strong lensing provides, with very few assumptions, a measurement of the projected mass of a galaxy integrated within an aperture to better than a few percent. Early-type galaxy (ETG) lenses in particular have allowed for a number of studies covering relevant topics of cosmology such as the density profile of ETGs (e.g., Rusin et al. 2003a,b; Koopmans & Treu 2004; Barnabè et al. 2011), the value of the Hubble constant and other cosmological parameters (e.g., Suyu et al. 2010, 2013; Gavazzi et al. 2008), the abundance of mass substructure in galaxies (e.g., Vegetti & Koopmans 2009), the stellar initial mass function (e.g., Treu et al. 2010; Ferreras et al.

2010) and the shape of dark matter halos (e.g., Sonnenfeld et al. 2012; Grillo 2012). The current number of known early-type galaxy lenses is above two hundred. While some of these lenses were serendipitous findings, most of them were discovered in the context of dedicated surveys. The largest such survey to date is the Sloan Lens ACS (SLACS) survey (Bolton et al. 2004), which provided about 80 lenses. Although this sample has yielded interesting results on the properties of ETGs, there are many astrophysical questions that can be better answered with a larger number of strong lenses spanning a larger volume in the space of relevant physical parameters. For instance, quantities like the dark matter fraction or the density slope of ETGs, measurable with lensing and stellar kinematics information, might be correlated with other observables such as the stellar mass or the effective radius. Moreover, the mass structure of ETGs could be evolving in time as a result of the mass accretion history. In order to test this scenario, a statistically significant number of lenses covering a range of redshift is needed. However, most of the galaxy-scale lenses known today are limited at a redshift $z < 0.3$, corresponding to a lookback time of about 3.4 Gyr.

One of the goals of the Strong Lensing Legacy Survey (SL2S) collaboration is to extend to higher redshifts the sample of known galaxy-scale gravitational lenses. In Papers I and II (Gavazzi et al. 2012; Ruff et al. 2011) we presented the pilot sample of 16 lenses. Here we extend

¹ Physics Department, University of California, Santa Barbara, CA 93106, USA

² Institut d’Astrophysique de Paris, UMR7095 CNRS - Université Pierre et Marie Curie, 98bis bd Arago, 75014 Paris, France

³ Kavli Institute for Particle Astrophysics and Cosmology, Stanford University, 452 Lomita Mall, Stanford, CA 94305, USA

⁴ Institute of Astronomy and Astrophysics, Academia Sinica, P.O. Box 23-141, Taipei 10617, Taiwan

⁵ Department of Physics, University of Oxford, Keble Road, Oxford, OX1 3RH, UK

* sonnen@physics.ucsb.edu

† Packard Research Fellow

our study to a sample of 56 objects at redshifts up to $z = 0.8$. In this paper we present the lensing models of the new systems along with revisited models of the old ones. Furthermore, we make more conservative assumptions about the intrinsic shape of the lensed sources by reconstructing them on a pixelized grid (Warren & Dye 2003; Suyu et al. 2006; Koopmans & Treu 2004). In a companion paper (Sonnenfeld et al. 2013, hereafter Paper IV) we include the stellar kinematic measurements and address the issue of the time evolution of the density profile of ETGs.

The goal of this paper is to present our new sample of lenses, characterize it in terms of Einstein radii and stellar masses, and to compare the effectiveness of ground-based versus space-based images for the purpose of confirming gravitational lens candidates. This paper, the third in the series, is organized as follows. Section 2 summarizes the SL2S and the associated Canada-France-Hawaii-Telescope Legacy Survey (CFHTLS) data, the lens detection method and the sample selection. In Section 3 we present all the photometric data set of the SL2S lenses, either coming from the CFHTLS parent photometry or from additional *Hubble Space Telescope* (*HST*) and Near infrared (IR) follow-up imaging. In Section 4 we describe the lens models of the 56 systems. In Section 5 we show measurements of the stellar mass of our lenses from stellar population synthesis fitting. We discuss and summarize our results in Section 6. Throughout this paper, magnitudes are given in the AB system. When computing distances, we assume a Λ CDM cosmology with matter and dark energy density $\Omega_m = 0.3$, $\Omega_\Lambda = 0.7$, and Hubble constant $H_0 = 70 \text{ km s}^{-1} \text{ Mpc}^{-1}$.

2. THE STRONG LENSING LEGACY SURVEY

SL2S (Cabanac et al. 2007) is a project dedicated to finding and studying galaxy-scale and group-scale strong gravitational lenses in the Canada France Hawaii Telescope Legacy Survey (CFHTLS). The main targets of this paper are massive red galaxies. The galaxy-scale SL2S lenses are found with a procedure described in detail in Paper I (Gavazzi et al. 2012) that can be summarized as follows. We scan the 170 square degrees of the CFHTLS with the automated software *RingFinder* (Gavazzi et al., in prep.) looking for tangentially elongated blue features around red galaxies. The lens candidates are then visually inspected and the most promising systems are followed up with *HST* and/or spectroscopy.

Previous papers have demonstrated the success of this technique. In Paper I (Gavazzi et al. 2012), we obtained lens models for a pilot sample of 16 lenses and in Paper II (Ruff et al. 2011), we combined this information with spectroscopic data to investigate the total mass density profile of the lens galaxies, and its evolution. Here we complete the sample by presenting all the new systems that have been followed-up with either high-resolution imaging or spectroscopy since the start of the campaign. We also re-analyze the pilot sample to ensure consistency. This paper is focused on the sample’s photometric data and lens models, while in Paper IV we present the corresponding spectroscopic observations, model the mass density profile of our lenses, and explore the population’s evolution with time.

SL2S is by no means the only systematic survey of massive galaxy lenses: two other large strong-lens samples

TABLE 1
CENSUS OF SL2S LENSES.

Grade	A	B	C	X	Total
With high-res imaging	30	3	13	21	67
With spectroscopy	36	15	2	5	58
High-res imaging and spectroscopy	27	3	0	0	30
Total with follow-up	39	15	15	26	95

NOTE. — Number of SL2S candidates for which we obtained follow-up observations in each quality bin. Grade A: definite lenses, B: probable lenses, C: possible lenses, X: non-lenses. We differentiate between lenses with spectroscopic follow-up, high-resolution imaging follow-up or any of the two. In bold font we give the numbers that add up to our overall sample size of 56.

are those of the SLACS (Bolton et al. 2004) and BELLS (BOSS Emission-Line Lensing Survey; Brownstein et al. 2012) survey. SL2S differs from SLACS and BELLS in the way lenses are found. While we look for lenses in wide-field imaging data, the SLACS and BELLS teams selected candidates by looking for spectroscopic signatures coming from two objects at different redshifts on the same line of sight in the Sloan Digital Sky Survey (SDSS) spectra. These two different techniques correspond to differences in the population of lenses in the respective samples. Given the relatively small fiber used in SDSS spectroscopic observations ($1''.5$ and $1''$ in radius, for SLACS and BELLS respectively), the spectroscopic surveys tend to select preferentially lenses with small Einstein radii, where both the arc from the lensed source and the deflector can be captured within the fiber. SL2S, on the other hand, finds with higher frequency lenses with Einstein radii above $1''$, since they can be more clearly resolved in ground-based images (even after the lensed sources have been deblended from the light of the central deflector). At a given redshift, different values of the Einstein radius correspond to different physical radii at which masses can be measured with lensing. For a quantitative estimate of the range of physical radii probed by the different surveys, we plot in Figure 1 the distribution of Einstein radii and the effective radii for lenses from SL2S (determined in Sections 3.1 and 4.1), BELLS (Brownstein et al. 2012) and SLACS (Auger et al. 2010), together with 5 lenses from the LSD study (Treu & Koopmans 2004). The different surveys complement each other nicely, each one providing independent information that cannot be easily gathered from the others.

In Table 1 we provide a census of SL2S targets that have been followed up so far. The systems are graded according to their subjective likelihood of being strong lenses: grade A are definite lenses, B are probable lenses, C are possible lenses or, more conservatively, systems for which the additional data set does not lead to conclusive answers about their actual strong lensing nature, and, grade X are non-lenses. Grades for individual systems are shown in Table 6 and discussed in Section 4.2.

In this paper we show detailed measurements of photometric properties, lens models and stellar masses for all grade A lenses and for all grade B and C systems with spectroscopic follow-up. The same selection criterion is applied in Paper IV.

3. PHOTOMETRIC OBSERVATIONS

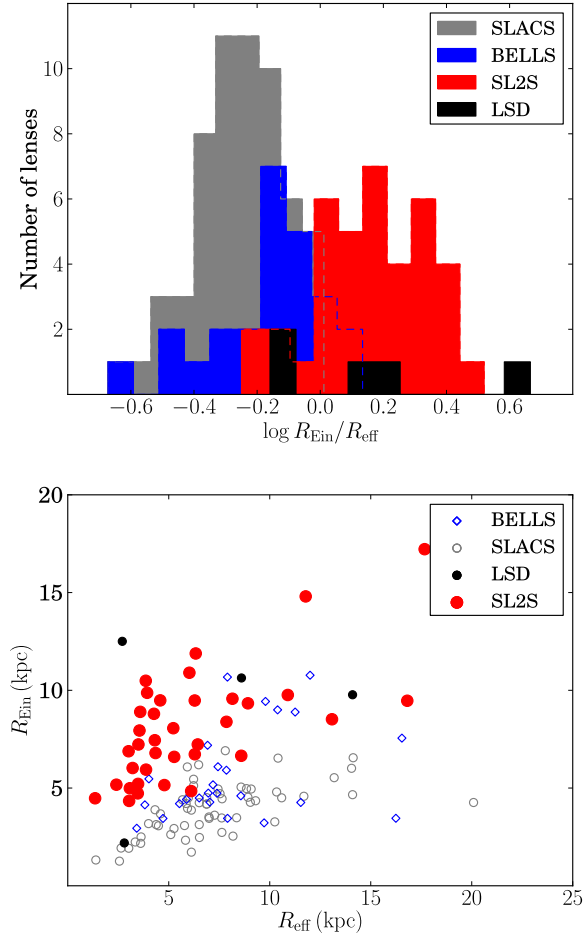


FIG. 1.— *Top Panel:* Distribution of Einstein radii, scaled by the effective radius, of lenses from SLACS (Auger et al. 2010), BELLS (Brownstein et al. 2012), LSD (Treu & Koopmans 2004) and grade-A SL2S. *Bottom Panel:* Same samples shown in the $R_{\text{Ein}}-R_{\text{eff}}$ plane.

All the SL2S lens candidates are first imaged by the CFHT as part of the CFHT Legacy Survey. CFHT optical images are taken with the instrument Megacam in the u, g, r, i, z filters under excellent seeing conditions. The typical FWHM in the g and i bands is $0''.7$. We refer to Gavazzi et al. (2012) for a more detailed description of ground-based optical observations.

The WIRCam (Puget et al. 2004) mounted on the CFHT was used to get Near IR follow-up photometry for some of the SL2S lens galaxies (Programs 11BF01, PI Gavazzi, and 07BF15 PI Soucail) or from existing surveys like WIRDS (Bielby et al. 2010, 2012)⁸ or from an ongoing one, called Miracles that is gathering a deep Near IR counter-part to a subset of the CFHTLS in the W1 and W4 fields (Arnouts et al., in prep). All these data were kindly reduced by the Terapix team.⁹ K_s (and sometimes also J and H) band is used for the systems listed in Table 2 to estimate more accurate stellar masses (see 5).

In addition to ground-based photometry, 33 of the

⁸ see also http://terapix.iap.fr/article.php?id_article=832

⁹ <http://terapix.iap.fr>

TABLE 2
SUMMARY OF NIR OBSERVATIONS

Name	Program	Filter	Exp. time (s)
SL2SJ021325-074355	11BF01	Ks	1050
SL2SJ021411-040502	07BF15	J,Ks	970,2480
SL2SJ021737-051329	07BF15	J,Ks	2470,1810
SL2SJ021902-082934	11BF01	Ks	1020
SL2SJ022357-065142	11BF01	Ks	1000
SL2SJ022511-045433	WIRDS	J,H,Ks	15720,11750,12860
SL2SJ022610-042011	WIRDS	J,H,Ks	13230,10240,11300
SL2SJ022648-040610	WIRDS	J,H,Ks	1800,820,1570
SL2SJ023251-040823	11BF01	Ks	1010
SL2SJ084909-041226	11BF01	Ks	1370
SL2SJ084959-025142	11BF01	Ks	1580
SL2SJ085826-014300	11BF01	Ks	1570
SL2SJ090106-025906	11BF01	Ks	1320
SL2SJ090407-005952	11BF01	Ks	1050
SL2SJ095921+020638	WIRDS	J,H,Ks	7500,16270,2990
SL2SJ220329+020518	11BF01	Ks	1840
SL2SJ220506+014703	MIRACLES	Ks	1140
SL2SJ220629+005728	MIRACLES	Ks	1340
SL2SJ221326-000946	11BF01	Ks	1280
SL2SJ221852+014038	MIRACLES	Ks	970
SL2SJ222012+010606	MIRACLES	Ks	1070
SL2SJ222148+011542	MIRACLES	Ks	250

TABLE 3
SUMMARY OF *HST* OBSERVATIONS

Set	Program	Instrument	Filter	Exp. time (s)
(a)	10876	ACS	F814W,F606W	800,400
(b)	11689	WFPC2	F606W	1200
(c)	11588	WFC3	F600LP,F475X	720
(d)	11588	WFC3	F475X	360

56 lens systems presented here have been observed with *HST* as part of programs 10876, 11289 (PI Kneib) and 11588 (PI Gavazzi), over the course of cycles 15, 16 and 17 respectively. A summary of *HST* observations is given in Table 3. The standard data reduction described in Paper I was performed.

3.1. Properties of lens galaxies

We wish to measure magnitudes, colors, effective radii, ellipticities and orientations of the stellar components of our lenses. This is done first by using the CFHT data, for all systems. We simultaneously fit for all the above parameters to the full set of images in the 5 optical filters, and NIR bands when available, by using the software *spasmoid*, developed by M. W. Auger and described in Bennert et al. (2011). Results are reported in Table 4. For systems with available *HST* data we repeat the fit using *HST* images alone. The measured parameters are reported in Table 5. Uncertainties on CFHT lens galaxy magnitudes are dominated by contamination from the background source and are estimated to be 0.3 in u band, 0.2 in g and r , 0.1 in all redder bands, while *HST* magnitudes have an uncertainty of 0.1. Although we used the same data, some of the CFHT magnitudes previously reported for the lenses studied in Paper I and Paper II are slightly inconsistent with the values measured

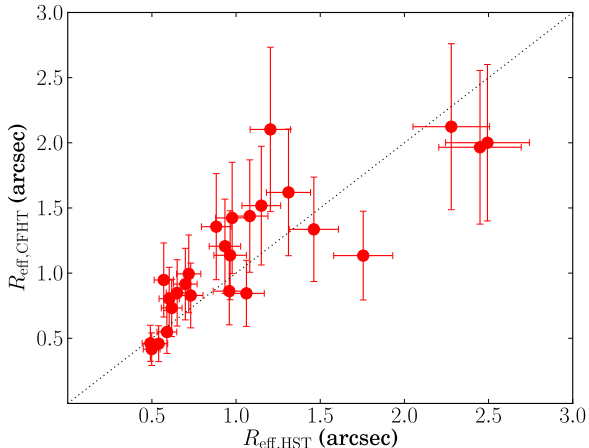


FIG. 2.— Comparison between effective radii measured from ground-based versus space-based photometry. Error bars on *HST* effective radii represent the assigned 10% systematic uncertainty due to fixing the light profile to a de Vaucouleurs model. The relative scatter between the best fit values of the two measurements is 30% and is used to quantify uncertainties in CFHT effective radii.

here. This difference is partly due to a different procedure in the masking of the lensed arcs. In Paper I and II, the lensed features were masked out automatically by clipping all the pixels more than 4σ above the best fit de Vaucouleurs profile obtained by fitting the deflector light distribution with *Galfit* (Peng et al. 2002, 2010), while here the masks are defined manually for every lens. We verified that this different approach is sufficient for causing the observed mismatch. The masking procedure adopted here is more robust and therefore we consider the new magnitudes more reliable. In addition, the measurements reported in Paper I and Paper II were allowing for different effective radii in different bands and the resulting magnitudes depend on the extrapolation of the light profile at large radii where the signal-to-noise ratio is extremely low. Here we fit for a unique effective radius in all bands, resulting in a more robust determination of relative fluxes, i.e. colors, important for the determination of stellar masses from photometry fitting. We note that this corresponds to an assumption of negligible intrinsic color gradient in the lens galaxies. However, asserting an effective radius that is constant across bandpasses mitigates against the much larger contamination from the lensed source.

Uncertainties on the *HST* effective radii are dominated by the choice of the model light profile: different models can fit the data equally well but give different estimates of R_{eff} . The dispersion is $\sim 10\%$, estimated by repeating the fit with a different surface brightness model, a Hernquist profile, and comparing the newly obtained values of R_{eff} with the de Vaucouleurs ones. Uncertainties on the CFHT effective radii are instead dominated by contamination from the background sources. Effective radii measured from CFHT images are in good agreement with those measured from *HST* data, when present, as shown in Figure 2. The scatter on the quantity $R_{\text{eff,CFHT}} - R_{\text{eff,HST}}$ is $\sim 30\%$; we take this as our uncertainty on CFHT effective radii.

4. LENS MODELS

The main goal is to measure Einstein radii of our lenses. We define the Einstein radius R_{Ein} to be the radius within which the mean surface mass density $\bar{\Sigma}(< R_{\text{Ein}})$ equals the critical density Σ_{cr} of the lensing configuration. While the critical density depends on the lens and source redshifts, the ratio of $\bar{\Sigma}(< R_{\text{Ein}})/\Sigma_{\text{cr}}$ (i.e., the convergence) does not: in practice then, the deflection angles and lensed image positions can all be predicted given a model with its Einstein radius in angular units. We only consider Einstein radii in angular units throughout this paper.

4.1. The method

We measure Einstein radii by fitting model mass distributions to the lensing data. We describe our lenses as singular isothermal ellipsoids (SIE), with convergence κ given by

$$\kappa(x, y) = \frac{R_{\text{Ein}}}{2r}, \quad (1)$$

where $r^2 \equiv qx^2 + y^2/q$ and q is the axis ratio of the elliptical isodensity contours. The free parameters of the lens model are therefore R_{Ein} , the axis ratio q , the position angle (PA) of the major axis, and the x and y positions of the centroid. In principle, more degrees of freedom could be introduced. In some cases, lens models are found to require a constant external shear, with strength γ_{ext} and position angle PA_{ext} , in order to describe the lensing effect of massive objects (such as groups or clusters) close to the optical axis. However, this external shear is highly degenerate with the mass orientation of the main lens, and our data are not detailed enough to distinguish between the two. For this reason we only include a shear component for the lenses that we cannot otherwise find a working model.

The fit is performed by generating model lensed images and comparing them to the observed images that have the lens light subtracted. For fixed lens parameters, light from the image plane is mapped back to a grid on the source plane and the source light distribution is then reconstructed following Suyu et al. (2006). This source reconstruction, as well as the entire lensing analysis, follows a Bayesian approach. For a given model lens, the Bayesian evidence of the source reconstruction is computed, which then defines the quality of the lens model. The lens parameter space is then explored with a Monte-Carlo Markov Chain (MCMC) sampler, propagating the source reconstruction evidence as the likelihood of the lens model parameters.

The practical realization of this procedure is done by using the lens modeling software *GLEE*, developed by Suyu & Halkola (2010). This approach differs slightly from the one adopted in Paper I, in that a pixelized source reconstruction is used instead of fitting Sérsic components. To make sure that our analysis is robust, we repeat the fit for the systems previously analyzed in Paper I. This allows us to gauge the importance of systematic effects related to the choice of modeling technique.

For systems with *HST* imaging in more than one band, only the bluest band image is used for the analysis as the signal from the blue star-forming lensed sources is highest. The g band image is used when modeling CFHT data. Typically we only attempt to model a small re-

TABLE 4
LENS LIGHT PARAMETERS, CFHT PHOTOMETRY.

Name	R_{eff} (arcsec)	q	PA (degrees)	u	g	r	i	z	J	H	Ks
SL2SJ020833-071414	1.06	0.81	61.1	22.71	20.64	18.99	18.22	17.90			
SL2SJ021206-075528	0.78	0.79	-29.2	23.33	21.32	19.75	18.90	18.61			
SL2SJ021247-055552	1.22	1.00	-9.1	23.59	22.73	21.44	20.21	19.77			
SL2SJ021325-074355	1.97	0.60	21.2	24.29	22.28	20.78	19.27	18.82			17.43
SL2SJ021411-040502	1.21	0.88	57.1	23.82	22.39	20.88	19.65	19.23	18.55		17.87
SL2SJ021737-051329	0.73	0.90	87.6	23.21	22.17	20.92	19.70	19.33	18.72		17.97
SL2SJ021801-080247	1.02	1.00	-49.8	23.05	22.07	21.32	20.33	19.64			
SL2SJ021902-082934	0.95	0.74	82.6	23.02	21.37	19.70	18.94	18.55			17.59
SL2SJ022046-094927	0.53	0.71	-68.5	24.17	22.33	20.88	19.88	19.52			
SL2SJ022056-063934	1.42	0.54	-74.8	21.65	19.85	18.47	17.86	17.59			
SL2SJ022346-053418	1.31	0.59	63.4	22.93	21.09	19.56	18.70	18.29			
SL2SJ022357-065142	1.36	0.95	37.2	23.13	21.03	19.42	18.63	18.30			17.45
SL2SJ022511-045433	2.12	0.72	27.5	20.32	18.58	17.36	16.81	16.55	15.99	15.64	15.48
SL2SJ022610-042011	0.84	0.87	52.0	23.30	21.28	19.70	18.80	18.46	18.09	17.70	17.38
SL2SJ022648-040610	0.48	0.30	-47.5	25.12	23.26	21.57	20.12	19.57	18.90	18.52	18.10
SL2SJ022648-090421	1.40	0.81	56.8	22.65	20.46	18.79	18.06	17.69			
SL2SJ023251-040823	1.14	0.70	-72.6	22.28	20.71	19.31	18.72	18.44			17.30
SL2SJ084847-035103	0.45	0.82	-65.4	24.57	23.57	22.16	20.81	20.39			
SL2SJ084909-041226	0.46	0.51	43.7	24.90	23.16	21.70	20.16	19.70			18.60
SL2SJ084934-043352	1.59	0.78	36.4	22.52	20.49	19.01	18.31	18.02			
SL2SJ084959-025142	1.34	0.79	-65.4	21.75	19.85	18.56	17.94	17.68			16.63
SL2SJ085019-034710	0.28	0.22	1.2	23.52	21.48	20.07	19.38	19.14			
SL2SJ085327-023745	1.47	0.81	-24.3	23.07	22.24	21.46	20.29	19.78			
SL2SJ085540-014730	0.69	0.82	-70.8	22.80	21.42	20.05	19.37	19.10			
SL2SJ085559-040917	1.13	0.82	23.1	23.18	21.10	19.48	18.72	18.35			
SL2SJ085826-014300	0.55	0.77	-86.2	24.09	23.15	21.85	20.78	20.38			19.20
SL2SJ090106-025906	0.42	0.82	-67.5	24.53	23.81	22.40	21.16	20.73			19.80
SL2SJ090407-005952	2.00	0.64	71.1	23.59	21.61	20.57	19.47	19.12			17.71
SL2SJ095921+020638	0.46	0.90	42.0	25.28	22.74	21.23	20.23	19.90	19.72	19.38	19.13
SL2SJ135847+545913	0.92	0.79	-72.4	23.93	21.66	20.14	19.16	18.78			
SL2SJ135949+553550	1.13	0.67	35.7	24.40	23.30	21.90	20.69	20.04			
SL2SJ140123+555705	0.86	0.75	-41.9	23.84	21.64	20.05	18.97	18.57			
SL2SJ140156+554446	1.44	0.82	20.2	23.07	20.83	19.28	18.47	18.02			
SL2SJ140221+550534	1.52	0.94	-18.1	22.28	20.47	18.89	18.19	17.82			
SL2SJ140454+520024	2.03	0.79	67.2	22.37	20.17	18.56	17.73	17.37			
SL2SJ140533+550231	0.56	0.67	15.8	24.32	22.48	21.10	20.13	19.62			
	1.11	0.98	-36.03	23.14	22.28	21.11	20.23	19.73			
SL2SJ140546+524311	0.83	0.89	-27.5	23.73	21.62	20.10	19.10	18.74			
SL2SJ140614+520253	2.21	0.50	-60.9	22.67	20.64	19.08	18.22	17.85			
SL2SJ140650+522619	0.80	0.67	87.4	23.84	22.59	21.31	19.96	19.47			
SL2SJ141137+565119	0.85	0.99	2.5	21.68	20.37	19.08	18.55	18.27			
SL2SJ141917+511729	2.10	0.64	47.7	23.33	20.96	19.43	18.56	18.21			
SL2SJ142003+523137	0.72	0.20	71.2	24.69	22.85	21.43	20.70	20.31			
SL2SJ142031+525822	1.11	0.62	-86.0	22.94	20.88	19.36	18.68	18.33			
SL2SJ142059+563007	1.62	0.54	-12.6	22.72	20.73	19.29	18.51	18.16			
SL2SJ142321+572243	1.42	0.82	62.9	23.67	21.65	20.00	18.95	18.64			
SL2SJ142731+551645	0.39	0.31	-63.7	23.33	22.00	20.74	19.85	19.47			
SL2SJ220329+020518	0.99	0.81	-44.7	22.68	21.08	19.80	19.15	18.83			17.85
SL2SJ220506+014703	0.66	0.48	87.2	23.71	21.69	20.09	19.24	18.92			17.73
SL2SJ220629+005728	1.37	0.63	-25.1	23.59	22.31	20.99	19.75	19.24			17.66
SL2SJ221326-000946	0.27	0.34	-29.1	23.60	21.78	20.33	19.74	19.44			18.61
SL2SJ221407-180712	0.68	0.72	57.0	24.81	22.81	21.37	20.15	19.73			
SL2SJ221852+014038	0.90	0.53	-67.1	23.86	21.70	20.19	19.07	18.67			17.54
SL2SJ221929-001743	1.01	0.78	85.1	21.32	19.52	18.31	17.78	17.50			
SL2SJ222012+010606	0.80	0.87	-22.4	22.34	20.47	19.38	18.84	18.56			17.69
SL2SJ222148+011542	1.12	0.81	79.6	22.02	20.15	18.83	18.21	17.91			16.90
SL2SJ222217+001202	1.56	0.66	37.7	22.77	21.03	19.62	18.88	18.53			

NOTE. — Best fit parameters for de Vaucouleurs models of the surface brightness profile of the lens galaxies, after careful manual masking of the lensed images. Columns 2–4 correspond to the effective radius (R_{eff}), the axis ratio of the elliptical isophotes (q), and the position angle measured east of north (PA). The system SL2SJ140533+550231 has two lens galaxies of comparable magnitude, and the parameters of both galaxies are given. The typical uncertainties are a few degrees for the position angle, $\Delta q \sim 0.03$ for the axis ratio, 0.3 for u -band magnitudes, 0.2 for g and r -band magnitudes, 0.1 for magnitudes in the remaining bands, 30% on the effective radii.

TABLE 5
LENS LIGHT PARAMETERS, *HST* PHOTOMETRY.

Name	R_{eff} (arcsec)	q	PA (degrees)	m_{F814W}	m_{F606W}	m_{F600LP}	m_{F475X}	Set
SL2SJ020833-071414	0.94	0.79	70.5	18.58	20.69	(c)
SL2SJ021325-074355	2.45	0.67	34.9	...	21.08	(b)
SL2SJ021411-040502	0.93	0.91	77.8	19.07	20.73	(a)
SL2SJ021737-051329	0.61	0.91	71.7	19.13	20.77	(a)
SL2SJ021902-082934	0.57	0.73	73.2	19.55	21.79	(c)
SL2SJ022357-065142	0.88	0.81	48.0	19.21	21.43	(c)
SL2SJ022511-045433	2.28	0.72	25.1	...	17.68	(b)
SL2SJ022610-042011	1.06	0.81	61.9	...	20.00	(b)
SL2SJ022648-040610	1.10	0.38	-47.4	...	21.45	(b)
SL2SJ023251-040823	0.96	0.74	-68.2	...	19.91	(b)
SL2SJ084909-041226	0.49	0.49	39.1	20.62	23.40	(c)
SL2SJ084959-025142	1.46	0.78	-64.1	...	18.80	(b)
SL2SJ085826-014300	0.59	0.81	82.2	...	22.22	(b)
SL2SJ090106-025906	0.50	0.80	-20.3	...	22.78	(b)
SL2SJ090407-005952	2.50	0.79	74.4	...	20.89	(b)
SL2SJ095921+020638	0.54	0.78	26.0	...	21.65	(b)
SL2SJ135847+545913	0.70	0.80	-57.1	19.65	21.99	(c)
SL2SJ135949+553550	1.76	0.61	30.7	...	22.01	(b)
SL2SJ140123+555705	0.96	0.78	-43.5	...	20.33	...	21.66	(b,d)
SL2SJ140156+554446	1.08	0.79	27.2	18.90	21.10	(c)
SL2SJ140221+550534	1.15	0.87	-43.9	18.59	20.63	(c)
SL2SJ140533+550231	0.91	0.75	-21.3	...	21.75	(b)
	0.41	0.93	-12.72	...	22.02	
SL2SJ140546+524311	0.73	0.82	-27.8	19.44	21.77	(c)
SL2SJ140650+522619	0.60	0.65	84.3	...	21.97	(b)
SL2SJ141137+565119	0.65	0.79	8.1	18.93	20.65	(c)
SL2SJ141917+511729	1.20	0.69	48.8	19.24	21.54	(c)
SL2SJ142031+525822	1.04	0.65	-80.0	...	19.86	(b)
SL2SJ142059+563007	1.31	0.58	-13.6	18.96	21.01	(c)
SL2SJ142321+572243	0.98	0.85	68.2	19.48	22.01	(c)
SL2SJ142731+551645	0.50	0.29	-62.1	...	21.08	(b)
SL2SJ220329+020518	0.72	0.84	-50.6	19.79	21.76	(c)
SL2SJ221326-000946	0.50	0.38	-32.5	...	20.64	(b)
SL2SJ221407-180712	0.77	0.69	49.1	...	21.69	(b)

NOTE. — Best fit parameters for de Vaucouleurs models of the surface brightness profile of the lens galaxies, after careful manual masking of the lensed images. Columns 2–4 correspond to the effective radius (R_{eff}), the axis ratio of the elliptical isophotes (q), and the position angle measured east of north (PA). The system SL2SJ140533+550231 has two lens galaxies of comparable magnitude, and the parameters of both galaxies are given. The last column indicates the set of observations used, from the list in Table 3.

gion of the image around the identified lensed sources, then check that our lens models do not predict detectable lensed sources in areas outside the data region. We assume uniform priors on all the lens parameters except the centroid, for which we use a Gaussian PDF centered on the observed light distribution and with a dispersion of 1 pixel. For systems with only ground-based imaging, for which the lensing signal is diluted by the large PSF, we keep the centroid fixed to that of the optimal light profile. In some cases we also adopt a Gaussian prior on the mass PA, centered on the PA of the light, or we keep the PA fixed. Those cases are individually discussed below.

Our analysis also allows us to determine the brightness of the lensed sources. This is important information as it allows us to constrain their distance in cases where their spectroscopic redshift is unknown (Ruff et al. 2011). The unlensed magnitude of the background object is recovered by fitting Sérsic components to the reconstructed source.

The values of the measured lens parameters with 68% credible intervals ($1 - \sigma$ uncertainties) derived from the posterior probability distribution marginalized over the remaining parameters are reported in Table 6. Cutouts of the lens systems with the most-probable image and source reconstruction are shown in Figure 3. All images are orientated north up and east left, with the exception of lens models based on WFPC2 data. Those models are performed in the native detector frame in order to avoid degrading further the quality of the WFPC2 images, as they typically have a low S/N. In such situations a compass is displayed to guide the eye.

The formal uncertainties on the Einstein radius given by the MCMC sampling are typically very small: the $1 - \sigma$ uncertainty is for most lenses smaller than 1%. However, our measurements of the Einstein radius rely partly on the assumption of an SIE profile for the lens mass distribution: in principle, mass models with density slope different from isothermal or isodensity contours different from ellipses can produce different Einstein radii. Perhaps more significantly, some systematic effects can be introduced at various points in our analysis: in particular, the assertions of a specific model PSF, a specific arc mask, and a specific lens light subtraction procedure all induce uncertainty in the final prepared data image (e.g. Marshall et al. 2007; Suyu et al. 2009). Bolton et al. (2008) estimated the systematic uncertainty on typical Einstein radius measurements to be about 2%. We can further verify this result by comparing Einstein radius measurements from paper I with the new values found here. The analysis of Paper I differs from the present one in the lens light subtraction, choice of the arc mask and lens model technique (Sérsic component fitting versus pixelized source reconstruction), so a comparison of the two different measurements should reflect systematics from most of the effects listed above. For a few of the systems already analyzed in Paper I, the current lens models are qualitatively different from the ones presented in Paper I and the measured values of the Einstein radii are correspondingly different. In most cases this is in virtue of the collection of new data with *HST* WFC3 that revealed features on the lensed arcs, previously undetected, that helped improve the lens model. After excluding those systems, the relative scatter between the

most probable values of R_{Ein} measured in the two different approaches (current and previous) is 3%. We thus take 3% as our estimate of the systematic uncertainty on the measurement of the Einstein radius with the technique used here, and convolve the posterior probability distribution for the Einstein radius obtained from the MCMC with a Gaussian with 3% dispersion. All the uncertainties on R_{Ein} quoted in this paper reflect this choice.

4.2. The lenses

Although the lens modeling procedure is the same for all lenses, each system has its own peculiarities that need to be taken care of. In what follows we describe briefly and case by case the relevant aspects of those lens models that deserve some discussion.

Lens grades are also discussed in this subsection, when explanation is needed, and are reported in Table 6. In general we apply the following guidelines. For a system with *HST* imaging we require, in order for it to be a grade A, that at least a pair of multiple images of the same source is visible and that we can describe it with a robust lens mass model compatible with the light distribution of the lens galaxy (i.e. similar centroid, orientation and axis ratio). For systems with only ground-based imaging we impose the additional requirement of having a spectroscopic detection of the background source, in order to be sure that the blue arcs that we observe are not part of the foreground galaxy. Spectroscopic data therefore enters the lens classification process. We refer to our companion paper (Paper IV) when discussing spectroscopic measurements. Furthermore, systems with a reliable ground-based lens model but no source spectroscopy are given grade B, as well as systems with secure spectroscopic detection of the source but no robust lens model. Systems lacking both, or for which we suspect that strong lensing might not be present are instead given grade C. We stress that a grade is not necessarily a statement on the quality or usefulness of a system as a lens, but rather its likelihood of being a strong lens given the available data. Consequently, grades are subject to change as new data become available.

- SL2SJ020833-071414. The lensed features of this system consist of a double image of a bright compact component and a low surface brightness ring. The model cannot fully reproduce the image of the bright double but this is probably due to the presence of a compact unresolved component, like an AGN. AGNs in the source plane are difficult to model with a pixelized reconstruction technique, because the image regularization process smoothes our model images. This effect is present in other lenses with sharp peaks in the source surface brightness distribution. Since the signal-to-noise ratio of the *HST* image is low and no additional information comes from spectroscopy, this lens is given a grade B.
- SL2SJ021325-074355. The source lensed by this high redshift galaxy ($z_d = 0.717$) appears to have two separate bright components. Our source reconstruction confirms this picture. There is a massive elliptical galaxy in the foreground that may be providing extra deflection to the light coming from the

- source, thus perturbing the image. This perturber is very close to the observer ($z = 0.0161$, from SDSS) and therefore its lensing power is greatly reduced with respect to the main deflector. We model the mass distribution from this galaxy with an additional SIE with centroid and PA fixed to the light distribution and R_{Ein} and q as free parameters. To quickly calculate the deflection angles from this perturber we make the approximation that it lies at the same redshift as the main lens. While this is not formally correct, the model still describes qualitatively the presence of an extra source of deflection towards the direction of the foreground galaxy. The impact of this perturber on the lensing model is in any case small.
- SL2SJ021411-040502. The source has two bright components, one of which is lensed into the big arc and its fainter counter-image. The second component forms a double of smaller magnification. This lens was modeled in Paper I where we explained how there are two lens models, with different Einstein radii, that match the image configuration. The pixelized source reconstruction technique adopted here to model the lens favors the solution alternative to the one chosen in Paper I.
 - SL2SJ021737-051329. This lens system is in a cusp configuration, meaning that the source lies just within one of the four cusps of the astroid caustic of the lens. Either a mass centroid offset from the light center or a large shear is required to match the curvature of the big arc. This was also needed in Paper I and previously found by Tu et al. (2009). Here, we find the amount of external shear to be $\gamma_{ext} = 0.11 \pm 0.01$
 - SL2SJ021801-010606. This system shows a nearly complete ring. The redshift of the blue component is 2.06 but we were not able to measure the redshift of the deflector, therefore we label this system as a grade B lens, needing follow-up with deeper spectroscopy.
 - SL2SJ022346-053418. The CFHT image shows an extended arc and a bright knot at the opposite side with respect to the lens. Although this latter component might be the counter-image to the arc, its color is different and it is not detected spectroscopically. Therefore only the arc is used for the lensing analysis. The main arc has a higher redshift than the lens, however the lens model is not definitive in assessing whether this system is a strong lens. This is therefore a grade B lens.
 - SL2SJ022357-065142. The lensed source appears to have a complex morphology. We identify three distinct components, each of which is doubly imaged.
 - SL2SJ084934-043352. Only one arc is visible in the CFHT image. In order to obtain a meaningful lens model we need to fix the PA of the mass profile to that of the light. This system is a grade B due to the lack of spectroscopic detection of the background source.
 - SL2SJ084959-025142 is a double-like lens system. Part of the light close to the smaller arc is masked out in our analysis, as it is probably a contamination from objects not associated with the lensed source.
 - SL2SJ085019-034710. The CFHT image shows a bright arc produced by the lensing effect of a disk galaxy. The lens model predicts the presence of a counter-image opposite to the arc, but it is not bright enough to be distinguished from the disk of the lens. In addition, such a counterimage could suffer from substantial extinction.
 - SL2SJ085559-040917. The main blue arc of this system is at redshift 2.95. The other blue features seen in CFHT data however are too faint for us to establish an unambiguous interpretation of the lens configuration. Therefore we conservatively assign grade B to this system. Higher resolution photometry is needed to confirm this lens.
 - SL2SJ090106-025906. The WFPC2 image of this system is contaminated with a cosmic ray, which has been masked out in our analysis. Our lens model predicts an image at the position of the cosmic ray, the presence of which cannot be verified with our data. The model however appears to be convincing and the background source is spectroscopically detected, therefore this is a grade A lens.
 - SL2SJ095921+020638. This system, belonging to the COSMOS survey had previously been modeled by Anguita et al. (2009). These authors report a source redshift of 3.14 ± 0.05 whereas we find a slightly greater value of 3.35 ± 0.01 based on our own XSHOOTER data (Paper IV). They report an Einstein radius $R_{Ein} \sim 0''.71$ in close agreement with our $0''.74 \pm 0''.04$ estimate.
 - SL2SJ135847+545913. We identify two distinct bright components in the source: one forms the big arc, the other one is only doubly-imaged.
 - SL2SJ140123+555705 is a cusp-like system: three images of a single bright knot can be identified on the arc. The counter-image however is too faint to be detected in the WFC3 snapshot. This lens was already modeled in Paper I. The Einstein radius that we obtain here is not consistent with the value reported then. This is because the current model is obtained by analyzing newly obtained WPC3 data, which reveal more details on the arc. The lack of a counterimage does not prevent an accurate lens modeling because the main arc is very thin, curved and extended.
 - SL2SJ140533+550231. This is a particular system, in that there are two lens galaxies of comparable brightness. The lensed image shows four images of a bright knot. We model the system with two SIE components, centered in correspondence with the two light components. Our inference shows a substantial degeneracy between the Einstein radii of the two lenses.

- SL2SJ140546+524311. This system shows a quadruply-imaged bright compact component. Two of the images are almost merged. A relatively large shear is required to match the position and shape of the counter-image opposite to the arcs.
- SL2SJ140614+520253. A few different blue blobs are visible in the CFHT image, but there is no working lens model that can associate them with the same source. As done in Paper I, we model only the bright extended arc. The resulting Einstein radius differs from the value of Paper I. This reflects the fact that the interpretation of this system as a lens is not straightforward. This is Grade B until future *HST* data shed more light on the actual nature of this system.
- SL2SJ140650+522619 has a cusp configuration. Even though the source appears to have two separate components, the compact structure outside of the main arc is actually a foreground object, as revealed by our spectroscopic observations.
- SL2SJ141137+565119 shows a complete ring. Our lens model cannot account for all the flux in one bright knot on the arc, North of the lens. This could be the result of the presence of substructure close to the highly magnified unresolved knot that requires a minute knowledge of the PSF.
- SL2SJ141917+511729. Only two bright points can be identified on the arc of this system, while no counter-image is visible. The Einstein radius of this lens is rather large ($\sim 4''$), which puts this system in the category of group-scale lenses.
- SL2SJ142003+523137. This disk galaxy is producing a lensed arc. The reconstructed source is compact and difficult to resolve. The predicted counter-image of the arc is too faint to be detected and possibly affected by extinction.
- SL2SJ142059+563007. The WFC3 image of this lens offers a detailed view on the source structure. We identify three separate bright components, two quads and one double, which allow us to constrain robustly the Einstein radius.
- SL2SJ142731+551645. The source lensed by this disky galaxy is in a typical fold-like configuration, with two of its four images merging into an arc.
- SL2SJ220329+020518. This system shows a bright arc, and a possible counter-image close to the center. However, we are not able to fit both the light from the arc and the candidate counter-image. On the other hand, our spectroscopic analysis reveals OII emission at the redshift of the lens (Paper IV), which suggests that the blue bright spot close to the center might be a substructure associated with the lens and not the source. We model the system using light from the arc only. Our model predicts the existence of a faint counter-image that cannot be ruled out by our snapshot observation.
- SL2SJ220506+014703. The spectroscopic follow-up revealed emission from the bright arc at $z = 2.52$. No emission is detected from its counter-image, but since the lens model is robust we give this lens a grade A.
- SL2SJ220629+005728. The image shows a secondary component with a color similar to the main lens, in the proximity of one of the arcs. This component could contribute to the overall lensing effect. We modeled it with a singular isothermal sphere. The fit yielded a small value for its Einstein radius as in Paper I.
- SL2SJ221326-000946 is a disky lens. A merging pair and a third image of the same bright component are identified on the arc. No counter-image is visible in our images.
- SL2SJ221407-180712. Analogous to other systems with CFHT data only, we need to fix the PA of the mass distribution in order to constrain accurately the Einstein radius. It is a grade B because of the lack of source spectroscopy.
- SL2SJ221929-001743. Only one source component, at a spectroscopic redshift of $z = 1.02$, is visible in the CFHT image. The constraints that this image provides on the lens model are not good enough and we need to fix the position angle of the mass to that of the light. The best-fit model does not predict multiple images. Grade B.
- SL2SJ222012+010606. The CFHT image shows two blue components on opposite sides of the lens. The brighter arc is measured to be at a higher redshift than the lens, while we have no spectroscopic information on the fainter blob. The lens model that we obtain is only partly satisfactory, because it predicts a mass centroid off by ~ 1.5 pixels from the light centroid. Moreover, the stellar mass and velocity dispersion of the foreground galaxy are unusually low in relation to the measured Einstein radius. It seems then plausible that the secondary source component is not a counter-image to the main arc. The foreground galaxy is definitely providing some lensing, but probably not strong. Grade C.
- SL2SJ222148+011542. Two arcs are visible both in photometry and in spectroscopy, making this a grade A lens.
- SL2SJ222217+001202. An arc with no clear counter-image is visible in the ground-based image of this lens. We put a Gaussian prior on the lens PA, centered on the light PA and with a 10 degree dispersion, in order to obtain a meaningful model of this lens. Grade B.

5. STELLAR MASSES

One of the goals of our study is to better understand the mass assembly of early-type galaxies over cosmic time. While gravitational lensing provides us with a precise measurement of the total mass enclosed within

TABLE 6
LENS MODEL PARAMETERS

Name	R_{Ein} (arcsec)	q	PA (degrees)	m_s (mag)	Grade	Notes	<i>HST</i> ?
SL2SJ020833-071414	2.66 ± 0.08	0.76 ± 0.01	59.2 ± 0.3	24.88	B		Y
SL2SJ021206-075528	1.24 ± 0.04	0.77 ± 0.02	-12.7 ± 3.1	24.72	B		N
SL2SJ021247-055552	1.27 ± 0.04	0.82 ± 0.04	-34.3 ± 3.5	25.11	A		N
SL2SJ021325-074355	2.39 ± 0.07	0.54 ± 0.01	17.8 ± 0.4	23.68	A		Y
comp. 2	0.74 ± 0.11	0.34 ± 0.34	53.6 (fixed)				
SL2SJ021411-040502	1.41 ± 0.04	0.59 ± 0.02	-84.0 ± 1.1	24.61	A		Y
SL2SJ021737-051329	1.27 ± 0.04	0.85 ± 0.02	-75.1 ± 3.3	24.06	A		Y
γ_{ext}	0.11 ± 0.01		1.0 ± 0.1				
SL2SJ021801-080247	1.00 ± 0.03	0.81 ± 0.03	39.9 ± 2.7	24.79	B		N
SL2SJ021902-082934	1.30 ± 0.04	0.80 ± 0.06	-82.4 ± 3.9	26.31	A		Y
SL2SJ022046-094927	1.00 ± 0.03	0.96 ± 0.02	-38.0 ± 9.8	24.15	B		N
SL2SJ022056-063934	1.19 ± 0.04	0.61 ± 0.04	-79.8 ± 2.5	24.57	B		N
SL2SJ022346-053418	1.22 ± 0.11	0.39 ± 0.09	70.5 ± 5.0	24.35	B		N
SL2SJ022357-065142	1.36 ± 0.04	0.79 ± 0.03	66.7 ± 2.6	24.73	A		Y
SL2SJ022511-045433	1.76 ± 0.05	0.58 ± 0.02	24.6 ± 0.4	23.61	A		Y
SL2SJ022610-042011	1.19 ± 0.04	0.79 ± 0.03	-10.1 ± 6.0	25.26	A		Y
SL2SJ022648-040610	1.29 ± 0.04	0.79 ± 0.07	-64.3 ± 7.5	25.93	A	disky	Y
SL2SJ022648-090421	1.56 ± 0.05	0.87 ± 0.03	73.6 ± 4.2	26.16	B		N
SL2SJ023251-040823	1.04 ± 0.03	0.94 ± 0.03	76.8 ± -60.9	24.36	A		Y
SL2SJ084847-035103	0.85 ± 0.07	0.77 ± 0.18	80.5 ± -57.5	23.83	A		N
SL2SJ084909-041226	1.10 ± 0.03	0.73 ± 0.03	40.5 ± 1.6	24.16	A		Y
SL2SJ084934-043352	1.23 ± 0.05	0.63 ± 0.12	36.4 (fixed)	23.87	B		N
SL2SJ084959-025142	1.16 ± 0.04	0.72 ± 0.04	-62.7 ± 2.3	25.85	A		Y
SL2SJ085019-034710	0.93 ± 0.03	0.44 ± 0.05	2.2 ± 3.7	25.59	A	disky	N
SL2SJ085327-023745	1.31 ± 0.04	0.72 ± 0.02	-0.4 ± 1.2	23.07	A		N
SL2SJ085540-014730	1.03 ± 0.04	0.96 ± 0.03	-64.4 ± 40.5	25.32	A		N
SL2SJ085559-040917	1.36 ± 0.10	0.31 ± 0.13	39.4 ± 10.0	24.14	B		N
SL2SJ085826-014300	0.90 ± 0.03	0.91 ± 0.04	65.0 ± 20.3	26.36	A		Y
SL2SJ090106-025906	1.03 ± 0.03	0.45 ± 0.02	-19.2 ± 1.2	25.68	A		Y
SL2SJ090407-005952	1.40 ± 0.04	0.64 ± 0.01	71.8 ± 0.8	24.32	A		Y
SL2SJ095921+020638	0.74 ± 0.02	0.95 ± 0.01	-72.0 ± 2.3	26.79	A		Y
SL2SJ135847+545913	1.21 ± 0.04	0.76 ± 0.01	-71.1 ± 1.6	24.30	A		Y
SL2SJ135949+553550	1.14 ± 0.03	0.60 ± 0.01	55.7 ± 0.5	25.53	A		Y
SL2SJ140123+555705	1.74 ± 0.07	0.49 ± 0.04	-43.8 ± 0.7	26.63	A		Y
SL2SJ140156+554446	2.03 ± 0.06	0.58 ± 0.01	32.1 ± 0.3	24.41	A		Y
SL2SJ140221+550534	1.23 ± 0.04	0.75 ± 0.04	-48.2 ± 3.0	25.41	A		Y
SL2SJ140454+520024	2.55 ± 0.08	0.55 ± 0.03	70.9 ± 0.8	24.79	A		N
SL2SJ140533+550231	1.05 ± 0.07	0.55 ± 0.02	1.7 ± 2.3	24.15	A	double	Y
comp. 2	0.52 ± 0.06	0.81 ± 0.06	42.1 ± 19.8				
SL2SJ140546+524311	1.51 ± 0.05	0.45 ± 0.04	-53.3 ± 2.3	26.44	A		Y
γ_{ext}	0.05 ± 0.02		-35.9 ± 0.1				
SL2SJ140614+520253	4.36 ± 0.16	0.64 ± 0.03	-52.5 ± 1.8	22.58	C		N
SL2SJ140650+522619	0.94 ± 0.03	1.00 ± 0.01	-26.8 ± 0.5	24.08	A		Y
SL2SJ141137+565119	0.93 ± 0.03	0.85 ± 0.01	62.4 ± 0.3	24.53	A		Y
SL2SJ141917+511729	3.11 ± 0.26	0.64 ± 0.12	49.5 ± 4.5	24.83	A		Y
SL2SJ142003+523137	1.79 ± 0.09	0.35 ± 0.03	65.6 ± 2.0	24.70	A	disky	N
SL2SJ142031+525822	0.96 ± 0.14	0.99 ± 0.12	-80.4 ± 5.3	22.45	B		Y
SL2SJ142059+563007	1.40 ± 0.04	0.67 ± 0.01	-10.4 ± 0.3	25.17	A		Y
SL2SJ142321+572243	1.30 ± 0.14	0.32 ± 0.03	43.9 ± 1.2	31.72	A		Y
SL2SJ142731+551645	0.81 ± 0.03	0.49 ± 0.02	-63.1 ± 0.9	24.73	A	disky	Y
SL2SJ220329+020518	1.95 ± 0.06	0.45 ± 0.01	-31.8 ± 0.2	24.95	A		Y
SL2SJ220506+014703	1.66 ± 0.06	0.74 ± 0.04	81.1 ± 3.4	23.68	A		N
SL2SJ220629+005728	1.55 ± 0.07	0.67 ± 0.04	-28.9 ± 3.8	24.78	B		N
comp. 2	0.16 ± 0.06						
SL2SJ221326-000946	1.07 ± 0.03	0.20 ± 0.01	-41.5 ± 0.5	24.82	A	disky	Y
SL2SJ221407-180712	1.06 ± 0.22	0.99 ± 0.09	57.0 (fixed)	25.01	B		N
SL2SJ221852+014038	1.38 ± 0.08	0.40 ± 0.09	-67.2 ± 4.9	25.54	B		N
SL2SJ221929-001743	0.52 ± 0.13	0.83 ± 0.30	85.1 (fixed)	23.46	B		N
SL2SJ222012+010606	2.16 ± 0.07	0.69 ± 0.03	-26.1 ± 3.0	24.09	C		N
SL2SJ222148+011542	1.40 ± 0.05	0.88 ± 0.03	77.7 ± 3.8	24.48	A		N
SL2SJ222217+001202	1.44 ± 0.15	0.82 ± 0.30	41.0 ± 6.8	24.83	B		N

NOTE. — Peak value and 68% confidence interval of the posterior probability distribution of each lens parameter, marginalized over the other parameters. Columns 2–4 correspond to the Einstein radius (R_{Ein}), the axis ratio of the elliptical isodensity contours (q), and the position angle measured east of north (PA) of the SIE lens model. Column 5 shows the magnitude of the de-lensed source in the band used for the lensing analysis: the bluest available band for *HST* data, or g band for CFHT data. The typical uncertainty on the source magnitude is ~ 0.5 . Column 6 lists notes on the lens morphology, while column 7 indicates whether the lens has *HST* imaging.

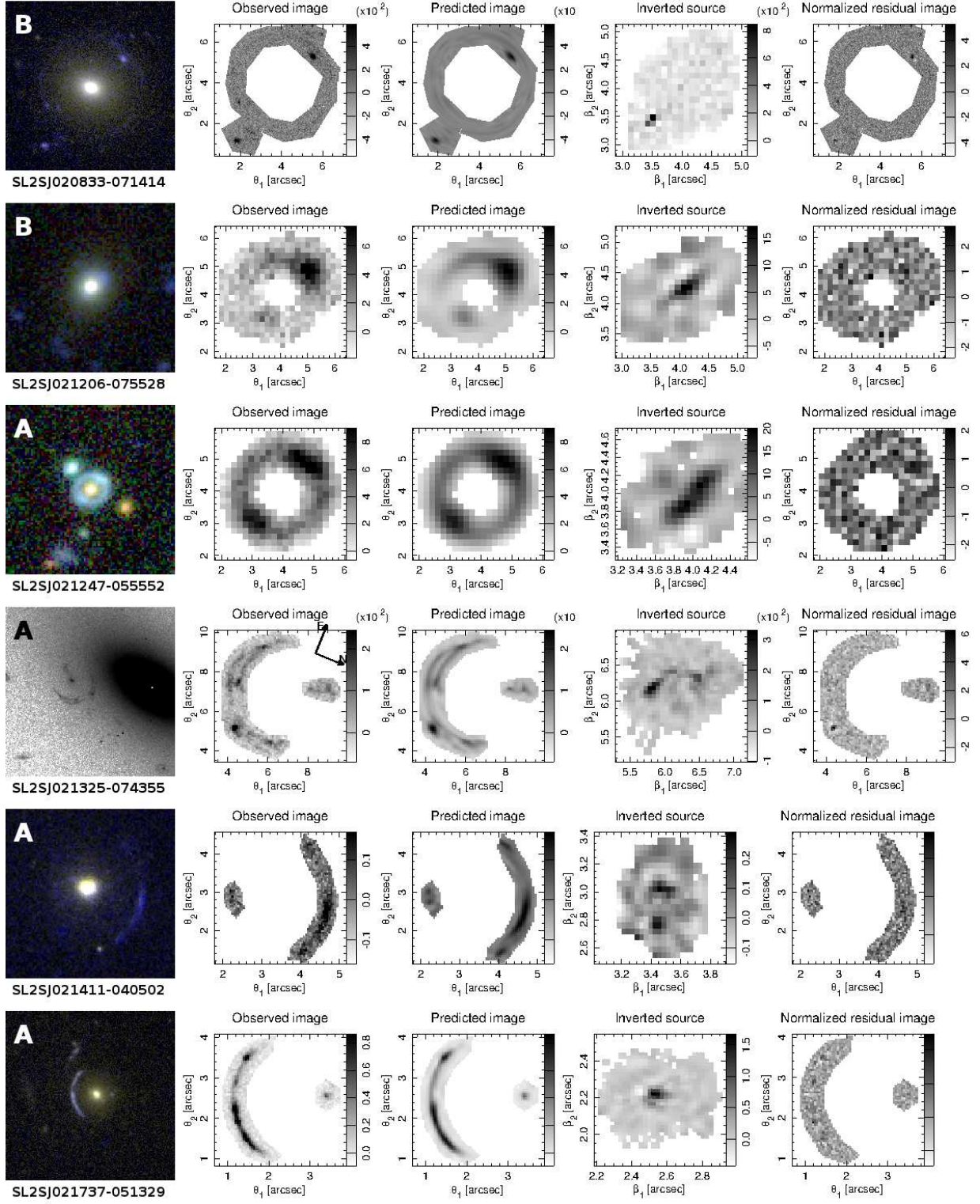


FIG. 3.— Lens modeling results showing, on each row, from left to right, a color cutout image, the input science imaged used for the modeling with uninteresting areas cropped out, the reconstructed lensed image, the reconstructed intrinsic source and the difference image (data–model) normalized in units of the estimated pixel uncertainties.

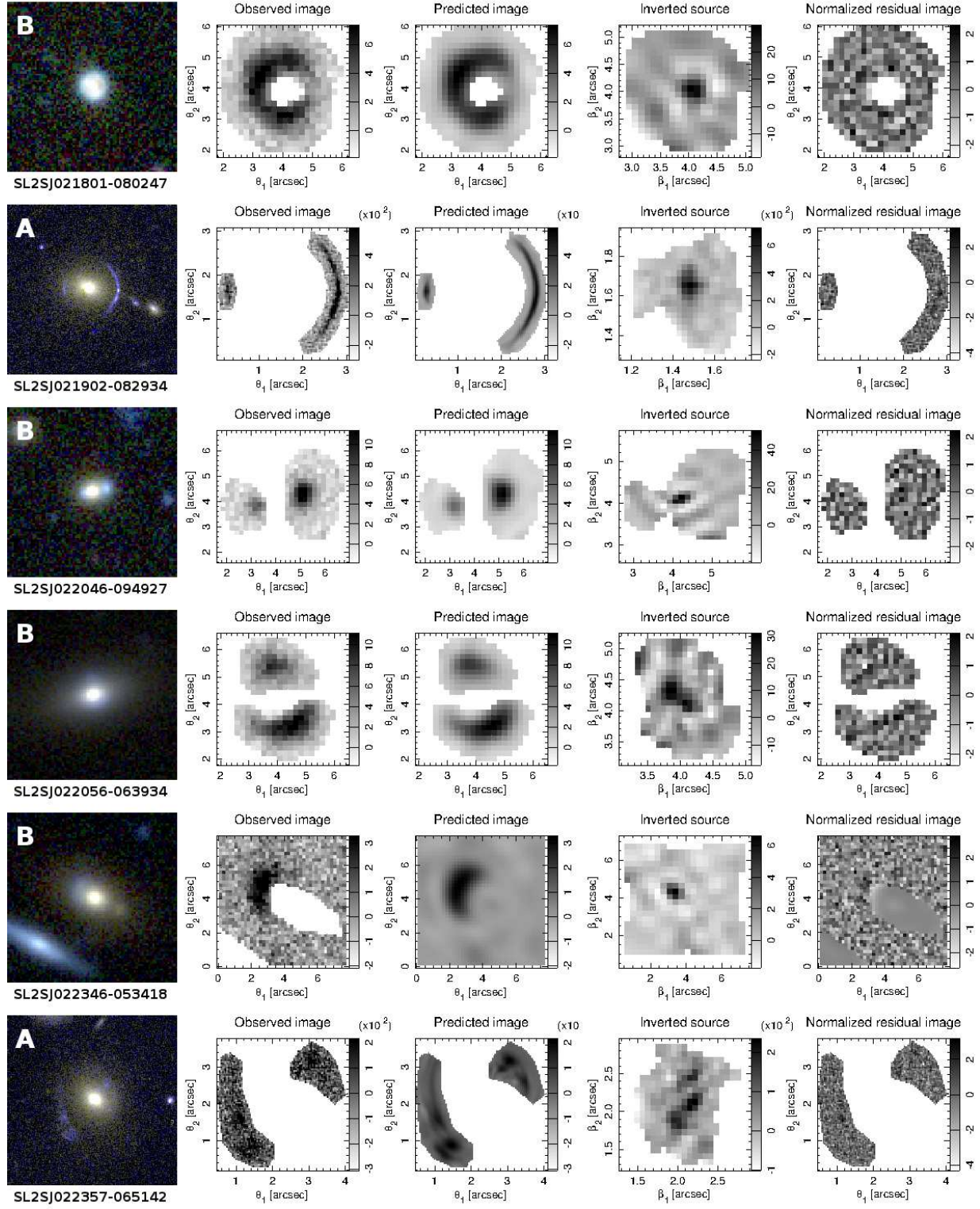


FIG. 3.— continued.

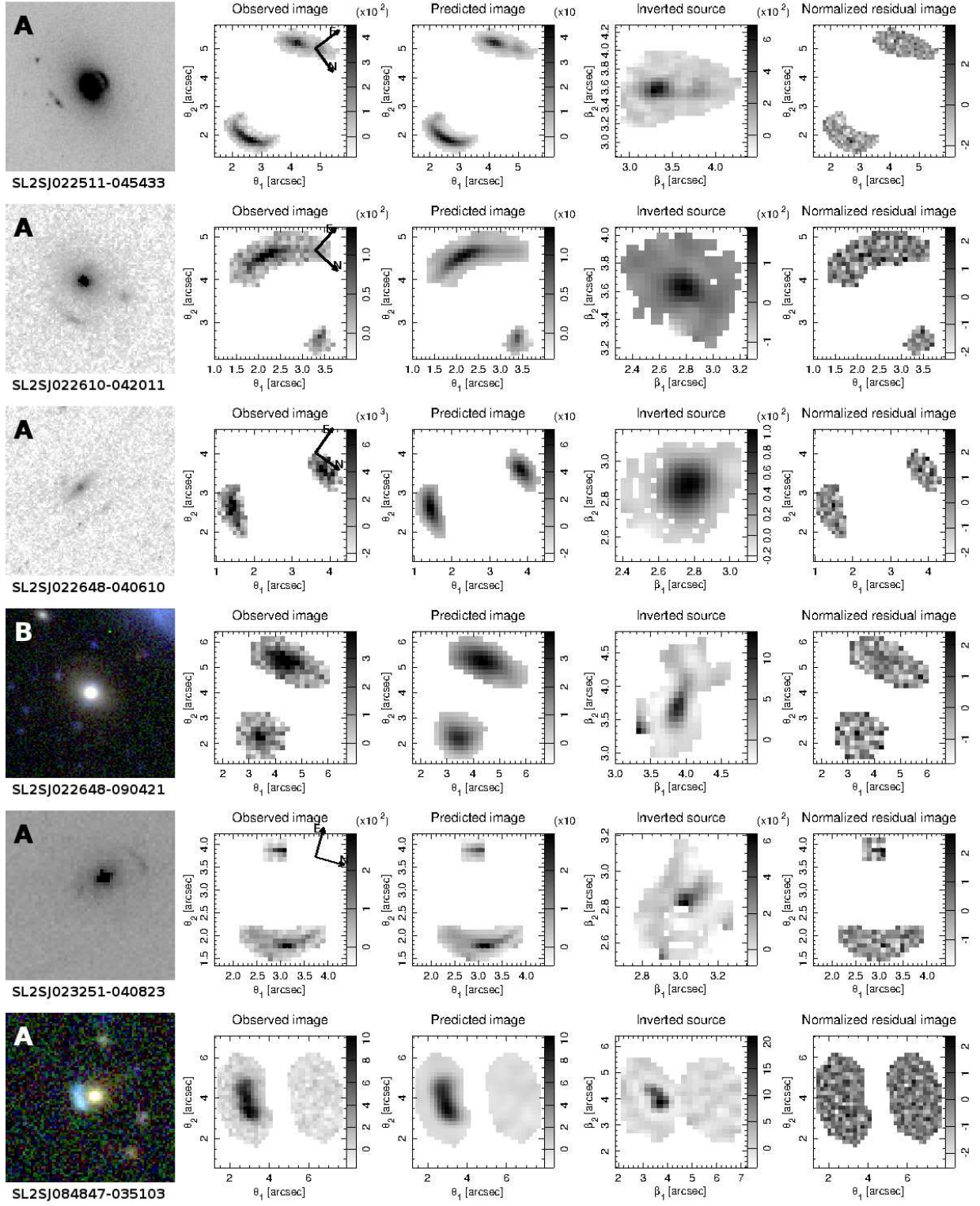


FIG. 3.— continued.

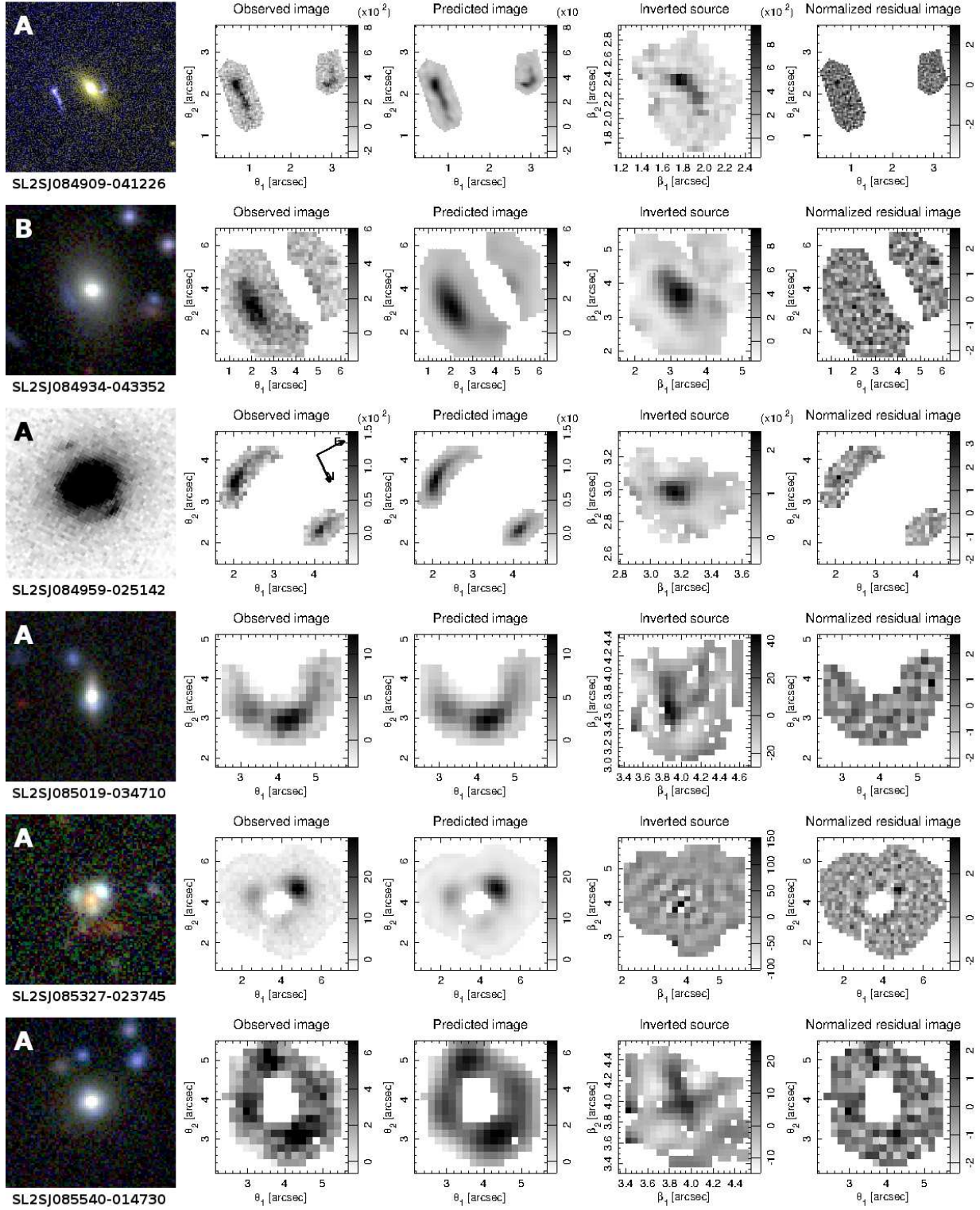


FIG. 3.— continued.

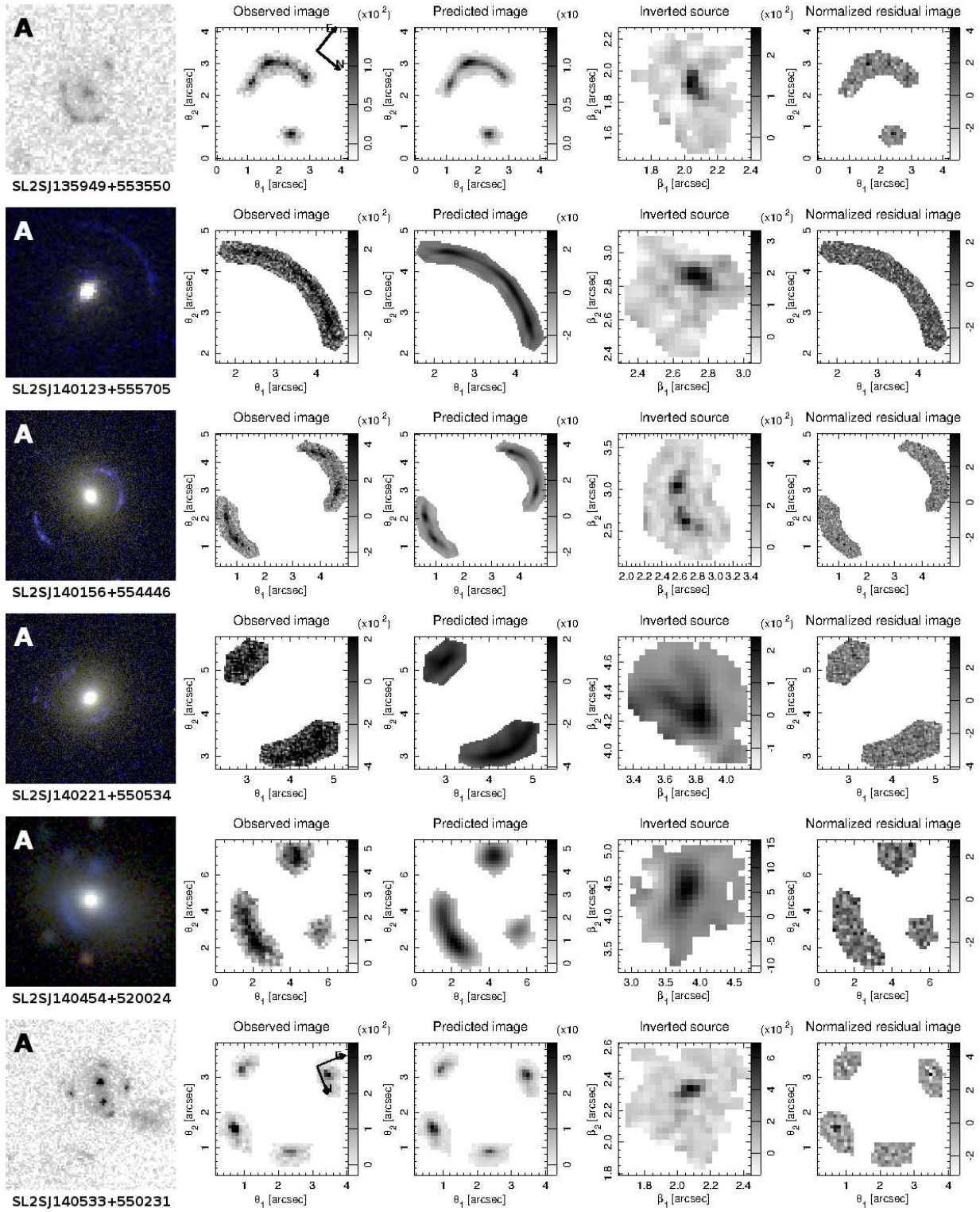


FIG. 3.— continued.

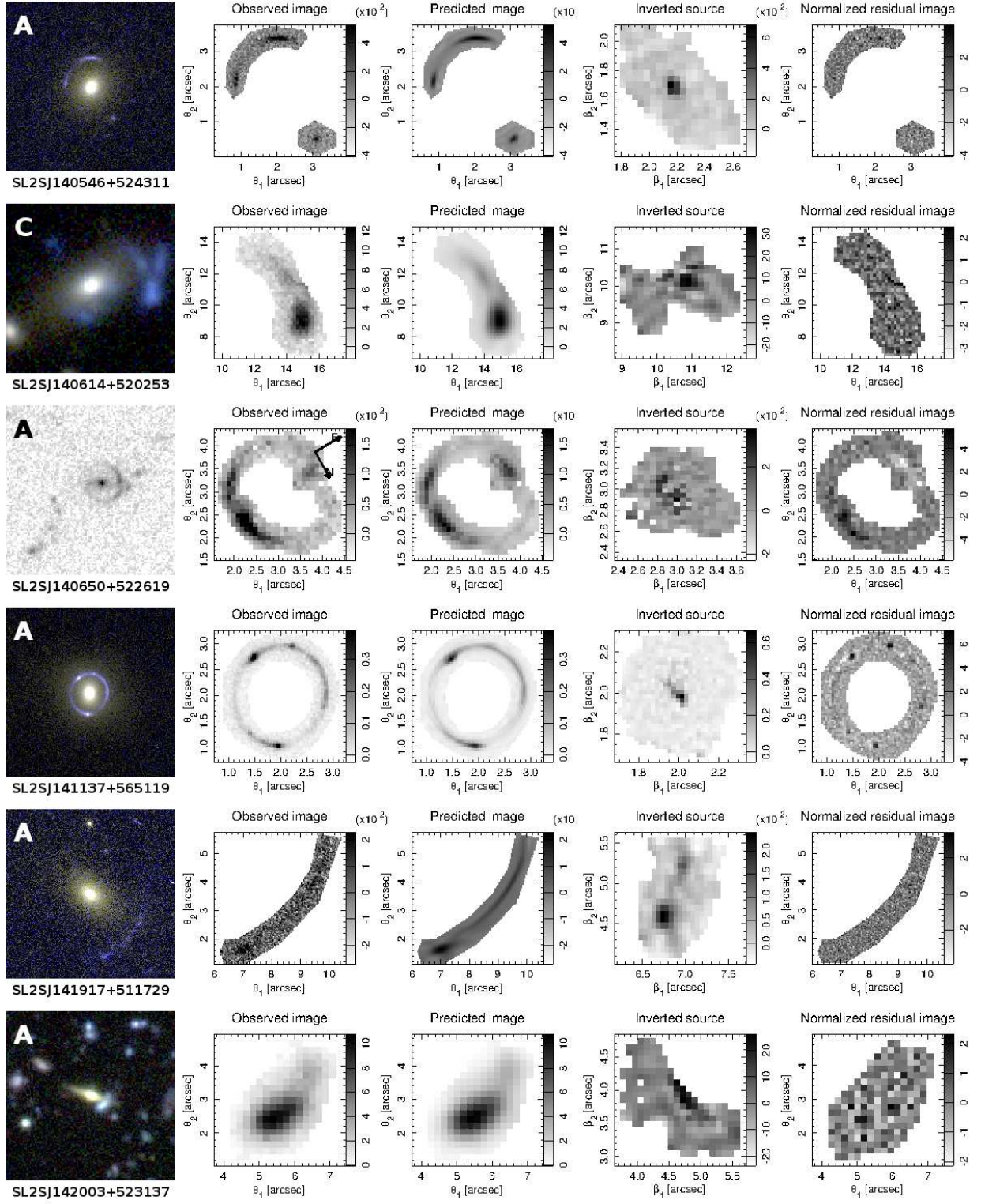


FIG. 3.— continued.

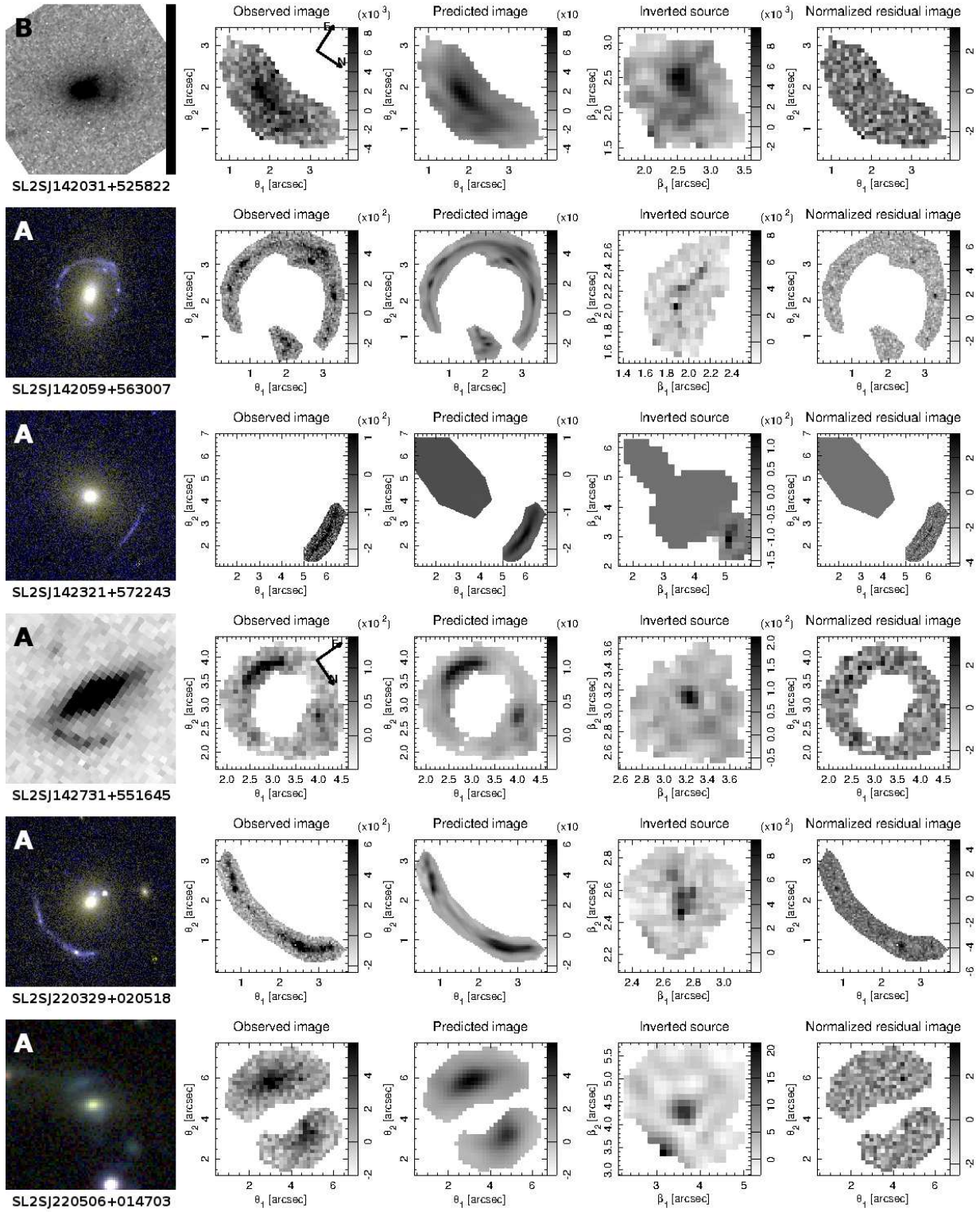


FIG. 3.— continued.

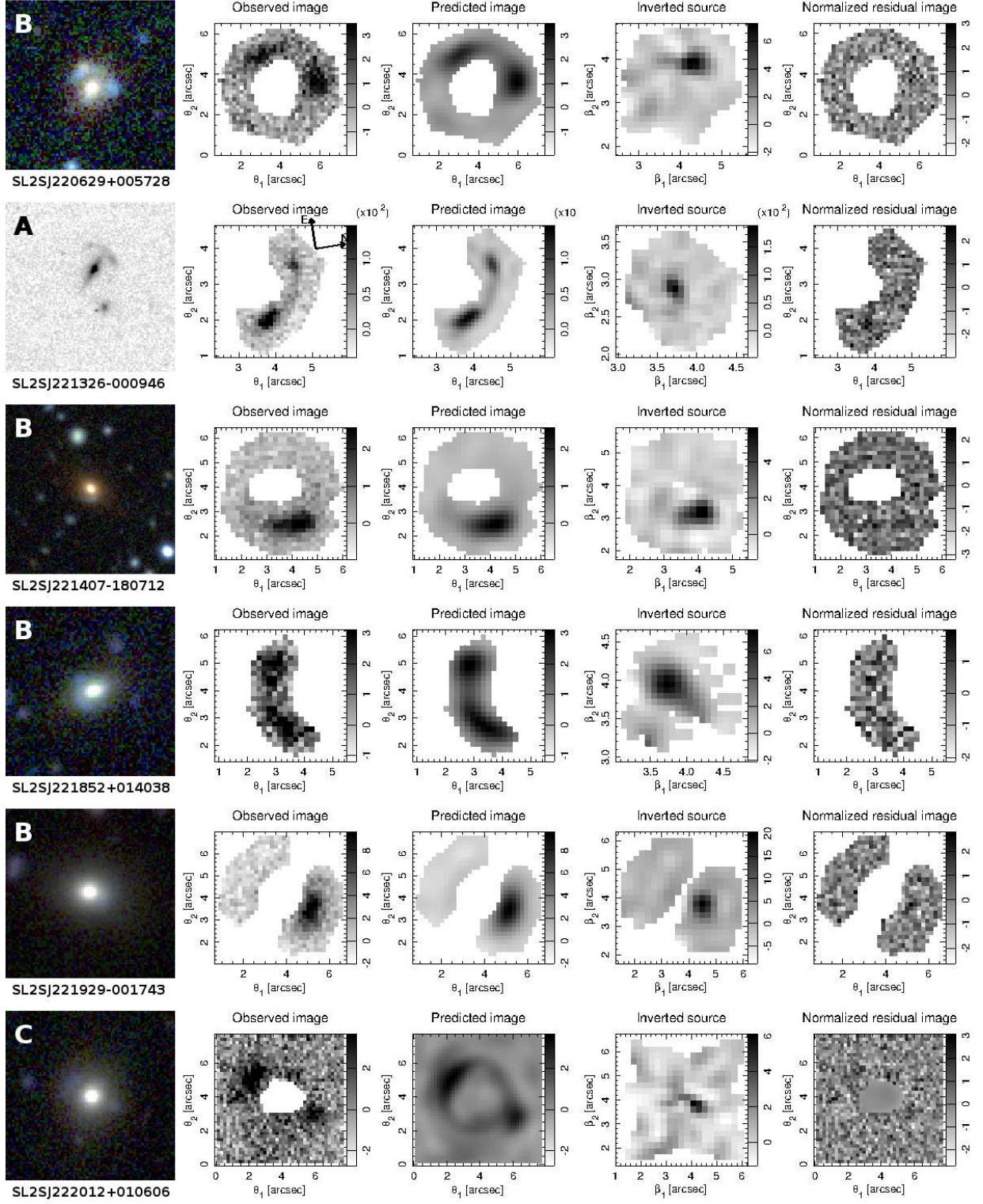


FIG. 3.— continued.

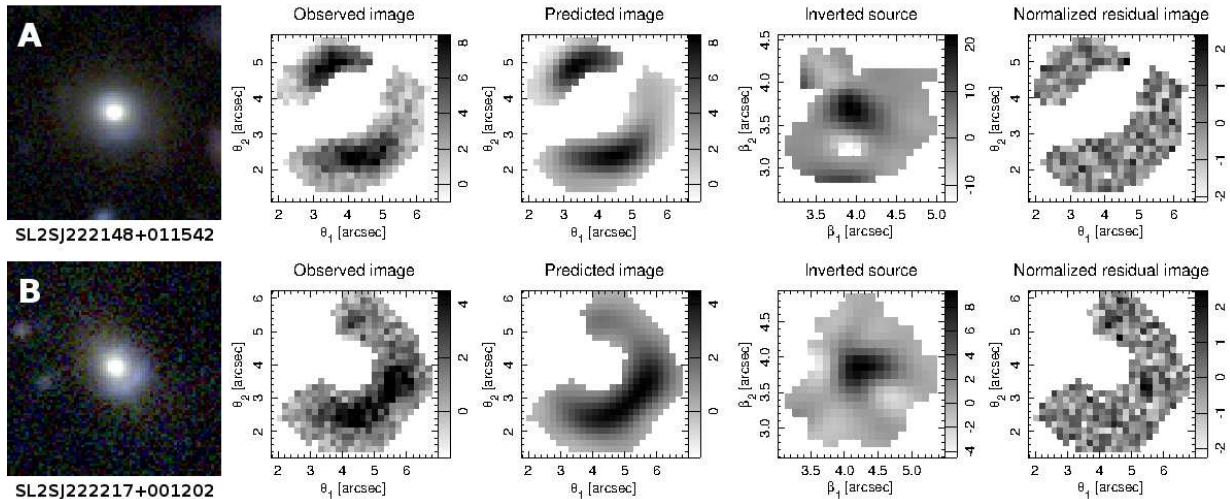


FIG. 3.— continued.

the Einstein radius of our lenses, measurements of the stellar mass are needed to separate the contribution of baryonic and dark matter to the total mass balance. In this paper we estimate stellar masses through stellar population synthesis (SPS) fitting of our photometric measurements: we create stellar populations assuming a simply-parametrized star formation history and stellar initial mass function (IMF), calculate magnitudes in the observed bands and fit to the measurements. The implementation of this procedure is the same as the one in Auger et al. (2009) and is based on a code written by M. W. Auger. We create composite stellar populations from stellar templates by Bruzual & Charlot (2003), with both a Salpeter and a Chabrier IMF. We assume an exponentially declining star formation history, appropriate given the old age of the red galaxies in our sample. In order to obtain robust stellar masses, measurements in a few different bands are needed. Although *HST* images provide better spatial resolution, useful to deblend the lens light from that of the background source, our objects have *HST* data in at most two bands which are not enough for the purpose of fitting SPS models. CFHT images on the other hand are deep and available consistently in five different bands for all of the targets. The inclusion of the *HST* photometry to the overall SED fitting would not bring much new information and we therefore discard it. The fit is based on an MCMC sampling. The measured values of the stellar masses are reported in Table 7.

For the systems with additional NIR observations the fit is repeated including those data. The addition of NIR fluxes produces stellar masses consistent with the values measured with optical data only, but with smaller uncertainty (see Figure 4). The relative scatter between stellar masses obtained from optical photometry alone and with the addition of NIR data is 0.06 dex in $\log M_*$ and the bias is 0.01. This gives us an estimate of the systematic error coming from the stellar templates being not a perfect description of the data over all photometric bands; in Paper IV, this systematic uncertainty is added to the statistical uncertainty on M_* when dealing with stellar masses. On the one hand the tight agreement between optical and optical+NIR stellar masses should not come as a surprise since the two data sets differ in most

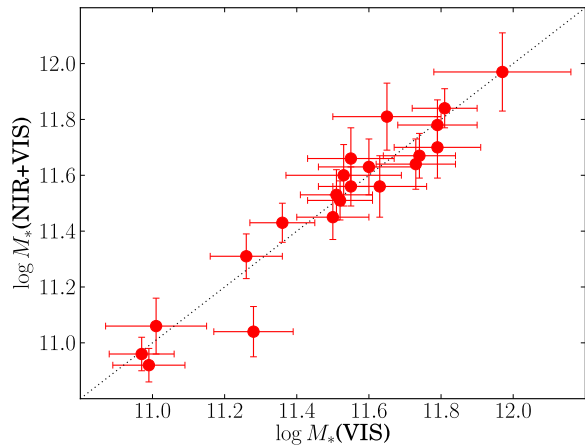


FIG. 4.— . Comparison of stellar masses obtained with either optical *ugriz* bands only or with optical + near IR bands, for a Salpeter IMF. We observe no significant differences in the recovered masses.

cases only by the addition of one band. On the other hand, if the optical data were contaminated with poor subtraction of light from the blue arcs the resulting stellar masses could be biased. The fact that NIR data, with little to no contamination from the background source, does not change the inference is reassuring on the quality of our photometric measurements.

Some of the stellar masses measured here are not consistent with previous measurements from Paper II. This reflects the difference in the measured magnitudes due to the different source masking strategy discussed in Section 3.1. The values reported here are to be considered more robust.

The median stellar mass of the sub-sample of grade A SL2S lenses is $10^{11.53} M_\odot$, if a Salpeter IMF is assumed, and the standard deviation of the sample is 0.3 dex in $\log M_*$. The distribution in stellar mass of SL2S galaxies is very similar to that of SLACS galaxies, as shown in Figure 5. This is important in view of analyses that combine data from both samples, as we do in Paper IV.

6. SUMMARY AND CONCLUSIONS

TABLE 7
STELLAR MASS MEASUREMENTS

Lens name	z	$\log M_*^{(\text{Chab})}/M_\odot$	$\log M_*^{(\text{Chab})}(\text{NIR})/M_\odot$	$\log M_*^{(\text{Salp})}/M_\odot$	$\log M_*^{(\text{Salp})}(\text{NIR})/M_\odot$
SL2SJ020833-071414	0.428	11.59 ± 0.10	...	11.84 ± 0.10	...
SL2SJ021206-075528	0.460	11.33 ± 0.10	...	11.59 ± 0.10	...
SL2SJ021247-055552	0.750	11.17 ± 0.17	...	11.45 ± 0.17	...
SL2SJ021325-074355	0.717	11.71 ± 0.18	11.73 ± 0.15	11.97 ± 0.19	11.97 ± 0.14
SL2SJ021411-040502	0.609	11.34 ± 0.14	11.38 ± 0.10	11.60 ± 0.14	11.63 ± 0.10
SL2SJ021737-051329	0.646	11.29 ± 0.15	11.35 ± 0.11	11.53 ± 0.16	11.60 ± 0.11
SL2SJ021801-080247
SL2SJ021902-082934	0.389	11.24 ± 0.10	11.20 ± 0.08	11.50 ± 0.10	11.45 ± 0.08
SL2SJ022046-094927	0.572	11.11 ± 0.12	...	11.36 ± 0.11	...
SL2SJ022056-063934	0.330	11.44 ± 0.10	...	11.69 ± 0.09	...
SL2SJ022346-053418	0.499	11.51 ± 0.11	...	11.76 ± 0.11	...
SL2SJ022357-065142	0.473	11.49 ± 0.10	11.44 ± 0.08	11.74 ± 0.10	11.67 ± 0.08
SL2SJ022511-045433	0.238	11.57 ± 0.09	11.59 ± 0.07	11.81 ± 0.09	11.84 ± 0.07
SL2SJ022610-042011	0.494	11.48 ± 0.10	11.41 ± 0.09	11.73 ± 0.11	11.64 ± 0.09
SL2SJ022648-040610	0.766	11.53 ± 0.12	11.46 ± 0.11	11.79 ± 0.12	11.70 ± 0.11
SL2SJ022648-090421	0.456	11.72 ± 0.10	...	11.97 ± 0.10	...
SL2SJ023251-040823	0.352	11.11 ± 0.10	11.18 ± 0.08	11.36 ± 0.09	11.43 ± 0.07
SL2SJ084847-035103	0.682	10.97 ± 0.16	...	11.24 ± 0.16	...
SL2SJ084909-041226	0.722	11.39 ± 0.14	11.31 ± 0.10	11.63 ± 0.13	11.56 ± 0.11
SL2SJ084934-043352	0.373	11.42 ± 0.10	...	11.67 ± 0.10	...
SL2SJ084959-025142	0.274	11.27 ± 0.09	11.27 ± 0.07	11.52 ± 0.09	11.51 ± 0.07
SL2SJ085019-034710	0.337	10.89 ± 0.09	...	11.14 ± 0.09	...
SL2SJ085327-023745	0.774	11.13 ± 0.16	...	11.38 ± 0.16	...
SL2SJ085540-014730	0.365	10.86 ± 0.10	...	11.11 ± 0.10	...
SL2SJ085559-040917	0.419	11.39 ± 0.10	...	11.63 ± 0.10	...
SL2SJ085826-014300	0.580	10.76 ± 0.14	10.81 ± 0.10	11.01 ± 0.14	11.06 ± 0.10
SL2SJ090106-025906	0.670	10.80 ± 0.17	...	11.07 ± 0.16	...
SL2SJ090407-005952	0.611	11.30 ± 0.11	11.41 ± 0.11	11.55 ± 0.12	11.66 ± 0.11
SL2SJ095921+020638	0.552	11.03 ± 0.10	10.81 ± 0.09	11.28 ± 0.11	11.04 ± 0.09
SL2SJ135847+545913	0.510	11.39 ± 0.11	...	11.66 ± 0.11	...
SL2SJ135949+553550	0.783	11.17 ± 0.15	...	11.41 ± 0.15	...
SL2SJ140123+555705	0.527	11.54 ± 0.11	...	11.80 ± 0.11	...
SL2SJ140156+554446	0.464	11.59 ± 0.10	...	11.85 ± 0.10	...
SL2SJ140221+550534	0.412	11.54 ± 0.10	...	11.79 ± 0.10	...
SL2SJ140454+520024	0.456	11.85 ± 0.10	...	12.10 ± 0.10	...
SL2SJ140533+550231
SL2SJ140546+524311	0.526	11.42 ± 0.11	...	11.67 ± 0.11	...
SL2SJ140614+520253	0.480	11.68 ± 0.11	...	11.93 ± 0.11	...
SL2SJ140650+522619	0.716	11.34 ± 0.15	...	11.60 ± 0.15	...
SL2SJ141137+565119	0.322	11.04 ± 0.09	...	11.28 ± 0.09	...
SL2SJ141917+511729
SL2SJ142003+523137	0.354	10.44 ± 0.10	...	10.69 ± 0.10	...
SL2SJ142031+525822	0.380	11.31 ± 0.10	...	11.56 ± 0.09	...
SL2SJ142059+563007	0.483	11.52 ± 0.10	...	11.76 ± 0.10	...
SL2SJ142321+572243
SL2SJ142731+551645	0.511	10.97 ± 0.12	...	11.20 ± 0.12	...
SL2SJ220329+020518	0.400	11.00 ± 0.09	11.05 ± 0.08	11.26 ± 0.10	11.31 ± 0.08
SL2SJ220506+014703	0.476	11.26 ± 0.11	11.29 ± 0.09	11.51 ± 0.10	11.53 ± 0.09
SL2SJ220629+005728	0.704	11.40 ± 0.15	11.56 ± 0.12	11.65 ± 0.15	11.81 ± 0.12
SL2SJ221326-000946	0.338	10.73 ± 0.09	10.67 ± 0.06	10.99 ± 0.10	10.92 ± 0.06
SL2SJ221407-180712	0.651
SL2SJ221852+014038	0.564	11.52 ± 0.11	11.52 ± 0.09	11.79 ± 0.11	11.78 ± 0.09
SL2SJ221929-001743	0.289	11.32 ± 0.09	...	11.56 ± 0.09	...
SL2SJ222012+010606	0.232	10.73 ± 0.10	10.72 ± 0.07	10.97 ± 0.09	10.96 ± 0.06
SL2SJ222148+011542	0.325	11.30 ± 0.09	11.31 ± 0.07	11.55 ± 0.09	11.56 ± 0.07
SL2SJ222217+001202	0.436	11.26 ± 0.10	...	11.50 ± 0.10	...

NOTE. — Stellar masses from the fit of stellar population synthesis models to photometric data. The redshift of the lens galaxies is reported in column (2) and extensively discussed in Paper IV.

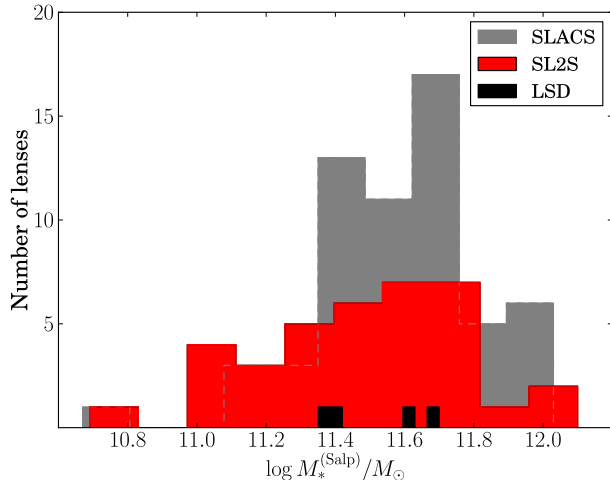


FIG. 5.— Distribution in stellar mass of the grade A SL2S, SLACS and LSD lenses. SLACS stellar masses are from Auger et al. (2010) and LSD masses are taken from Ruff et al. (2011). Stellar masses are obtained assuming a Salpeter IMF.

We presented photometric measurements, lens models and stellar mass measurements for a sample of 56 systems, of which 39 are grade A (definite lenses) and 15 are grade B (probable lenses). We find that *HST* imaging, even in snapshot mode, offers a clear-cut way to determine whether SL2S candidates are actual lenses. Not surprisingly, most grade A lenses are found for systems with *HST* data. 13 of the systems with high-resolution imaging are labeled as grade C lenses, meaning that their nature is undetermined. The data for these systems, not shown in this paper, come largely from WFPC2 snapshot observations. The signal-to-noise ratio of these WFPC2 images is low compared to images taken with ACS or WFC3 despite the longer exposure times. Most of the remaining grade C systems are targets observed with NIR photometry and adaptive optics, which proved not to be a very useful technique for the follow-up of our candidates.

Ground-based data can be used in some cases to construct lens models and measure precise Einstein radii: 9 out of 23 lenses with only CFHT photometry are grade A lenses. The uncertainty on R_{Ein} for those lenses is still dominated by the 3% systematic error, meaning that ground based photometry can sometimes be as good as space based imaging for the purpose of measuring Einstein radii. For most systems however the information is not enough to draw definite conclusions on their nature, and in a few cases the data does not offer enough constraints to measure Einstein radii, mostly because of the difficulty in detecting and exploiting the counterimage as seen from the ground. The range in Einstein radii covered by the grade A lenses in our sample is 5 – 15 kpc, typically larger than those of other surveys such as SLACS, probing the mass in regions where the contribution of dark matter is larger.

Stellar masses of lens galaxies can be measured from ground-based data. Measurements of M_* are robust to

the inclusion of NIR data. NIR should give more reliable stellar masses, since the blue background sources contribute very little to the infrared flux. Our result suggests that our measurements of the optical photometry of our lenses have little contamination from the background sources, and that we effectively deblended lens and source light. Stellar masses of SL2S lenses cover the range $10^{11} - 10^{12} M_\odot$, corresponding to massive ETGs.

In Paper IV we use all these measurements to put constraints on the mass profile of massive early-type galaxies and its evolution in the redshift range $0.1 < z < 0.8$.

We thank our friends of the SLACS and SL2S collaborations for many useful and insightful discussions over the course of the past years. We thank V.N. Bennert and M. Bradac for their help in our observational campaign. TT thanks S.W. Allen and B. Poggianti for useful discussions. RG acknowledges support from the Centre National des Etudes Spatiales (CNES). PJM acknowledges support from the Royal Society in the form of a research fellowship. TT acknowledges support from the NSF through CAREER award NSF-0642621, and from the Packard Foundation through a Packard Research Fellowship. This research is based on XSHOOTER observations made with ESO Telescopes at the Paranal Observatory under programme IDs 086.B-0407(A) and 089.B-0057(A). This research is based on observations obtained with MegaPrime/MegaCam, a joint project of CFHT and CEA/DAPNIA, and with WIRCam, a joint project of CFHT, Taiwan, Korea, Canada and France, at the Canada-France-Hawaii Telescope (CFHT) which is operated by the National Research Council (NRC) of Canada, the Institut National des Sciences de l'Univers of the Centre National de la Recherche Scientifique (CNRS) of France, and the University of Hawaii. This work is based in part on data products produced at TERAPIX and the Canadian Astronomy Data Centre. The authors would like to thank S. Arnouts, L. Van waerbeke and G. Morrison for giving access to the WIRCam data collected in W1 and W4 as part of additional CFHT programs. We are particularly thankful to Terapix for the data reduction of this dataset. This research is supported by NASA through Hubble Space Telescope programs GO-10876, GO-11289, GO-11588 and in part by the National Science Foundation under Grant No. PHY99-07949, and is based on observations made with the NASA/ESA Hubble Space Telescope and obtained at the Space Telescope Science Institute, which is operated by the Association of Universities for Research in Astronomy, Inc., under NASA contract NAS 5-26555, and at the W.M. Keck Observatory, which is operated as a scientific partnership among the California Institute of Technology, the University of California and the National Aeronautics and Space Administration. The Observatory was made possible by the generous financial support of the W.M. Keck Foundation. The authors wish to recognize and acknowledge the very significant cultural role and reverence that the summit of Mauna Kea has always had within the indigenous Hawaiian community. We are most fortunate to have the opportunity to conduct observations from this mountain.

REFERENCES

- Anguita, T., Faure, C., Kneib, J.-P., Wambsganss, J., Knobel, C., Koekemoer, A. M., & Limousin, M. 2009, *A&A*, 507, 35
- Auger, M. W., Treu, T., Bolton, A. S., Gavazzi, R., Koopmans, L. V. E., Marshall, P. J., Bundy, K., & Moustakas, L. A. 2009, *ApJ*, 705, 1099

- Auger, M. W., Treu, T., Bolton, A. S., Gavazzi, R., Koopmans, L. V. E., Marshall, P. J., Moustakas, L. A., & Burles, S. 2010, *ApJ*, 724, 511
- Barnabè, M., Czoske, O., Koopmans, L. V. E., Treu, T., & Bolton, A. S. 2011, *MNRAS*, 415, 2215
- Bennert, V. N., Auger, M. W., Treu, T., Woo, J.-H., & Malkan, M. A. 2011, *ApJ*, 726, 59
- Bielby, R., Hudelot, P., McCracken, H. J., Ilbert, O., Daddi, E., Le Fèvre, O., Gonzalez-Perez, V., Kneib, J.-P., Marmo, C., Mellier, Y., Salvato, M., Sanders, D. B., & Willott, C. J. 2012, *A&A*, 545, A23
- Bielby, R. M., Finoguenov, A., Tanaka, M., McCracken, H. J., Daddi, E., Hudelot, P., Ilbert, O., Kneib, J. P., Le Fèvre, O., Mellier, Y., Nandra, K., Petitjean, P., Srianand, R., Stalin, C. S., & Willott, C. J. 2010, *A&A*, 523, A66
- Bolton, A. S., Burles, S., Koopmans, L. V. E., Treu, T., Gavazzi, R., Moustakas, L. A., Wayth, R., & Schlegel, D. J. 2008, *ApJ*, 682, 964
- Bolton, A. S., Burles, S., Schlegel, D. J., Eisenstein, D. J., & Brinkmann, J. 2004, *AJ*, 127, 1860
- Brownstein, J. R., Bolton, A. S., Schlegel, D. J., Eisenstein, D. J., Kochanek, C. S., Connolly, N., Maraston, C., Pandey, P., Seitz, S., Wake, D. A., Wood-Vasey, W. M., Brinkmann, J., Schneider, D. P., & Weaver, B. A. 2012, *ApJ*, 744, 41
- Bruzual, G., & Charlot, S. 2003, *MNRAS*, 344, 1000
- Cabanac, R. A., Alard, C., Dantel-Fort, M., Fort, B., Gavazzi, R., Gomez, P., Kneib, J. P., Le Fèvre, O., Mellier, Y., Pello, R., Soucaïl, G., Sygnet, J. F., & Valls-Gabaud, D. 2007, *A&A*, 461, 813
- Ferreras, I., Saha, P., Leier, D., Courbin, F., & Falco, E. E. 2010, *MNRAS*, 409, L30
- Gavazzi, R., Treu, T., Koopmans, L. V. E., Bolton, A. S., Moustakas, L. A., Burles, S., & Marshall, P. J. 2008, *ApJ*, 677, 1046
- Gavazzi, R., Treu, T., Marshall, P. J., Brault, F., & Ruff, A. 2012, *ApJ*, 761, 170
- Grillo, C. 2012, *ApJ*, 747, L15
- Koopmans, L. V. E., & Treu, T. 2004, in *Astrophysics and Space Science Library*, Vol. 301, *Astrophysics and Space Science Library*, ed. M. Plionis, 23
- Marshall, P. J., et al. 2007, *ApJ*, 671, 1196
- Peng, C. Y., Ho, L. C., Impey, C. D., & Rix, H.-W. 2002, *AJ*, 124, 266
- . 2010, *AJ*, 139, 2097
- Puget, P., Stadler, E., Doyon, R., Gigan, P., Thibault, S., Luppino, G., Barrick, G., Benedict, T., Forveille, T., Rambold, W., Thomas, J., Vermeulen, T., Ward, J., Beuzit, J.-L., Feautrier, P., Magnard, Y., Mella, G., Preis, O., Vallee, P., Wang, S.-y., Lin, C.-J., Hall, D. N., & Hodapp, K. W. 2004, in *Society of Photo-Optical Instrumentation Engineers (SPIE) Conference Series*, Vol. 5492, *Society of Photo-Optical Instrumentation Engineers (SPIE) Conference Series*, ed. A. F. M. Moorwood & M. Iye, 978–987
- Ruff, A. J., Gavazzi, R., Marshall, P. J., Treu, T., Auger, M. W., & Brault, F. 2011, *ApJ*, 727, 96
- Rusin, D., Kochanek, C. S., & Keeton, C. R. 2003a, *ApJ*, 595, 29
- Rusin, D., et al. 2003b, *ApJ*, 587, 143
- Sonnenfeld, A., Treu, T., Gavazzi, R., Marshall, P. J., Auger, M. W., Suyu, S. H., Koopmans, L. V. E., & Bolton, A. S. 2012, *ApJ*, 752, 163
- Sonnenfeld, A., Treu, T., Gavazzi, R., Suyu, S. H., Marshall, P. J., Auger, M. W., & Nipoti, C. 2013, submitted to *ApJ*, available at [http://web.physics.ucsb.edu/~sim\\$sonnen/SL2S-IV.pdf](http://web.physics.ucsb.edu/~sim$sonnen/SL2S-IV.pdf)
- Suyu, S. H., Auger, M. W., Hilbert, S., Marshall, P. J., Tewes, M., Treu, T., Fassnacht, C. D., Koopmans, L. V. E., Sluse, D., Blandford, R. D., Courbin, F., & Meylan, G. 2013, *ApJ*, 766, 70
- Suyu, S. H., & Halkola, A. 2010, *A&A*, 524, A94
- Suyu, S. H., Marshall, P. J., Auger, M. W., Hilbert, S., Blandford, R. D., Koopmans, L. V. E., Fassnacht, C. D., & Treu, T. 2010, *ApJ*, 711, 201
- Suyu, S. H., Marshall, P. J., Blandford, R. D., Fassnacht, C. D., Koopmans, L. V. E., McKean, J. P., & Treu, T. 2009, *ApJ*, 691, 277
- Suyu, S. H., Marshall, P. J., Hobson, M. P., & Blandford, R. D. 2006, *MNRAS*, 371, 983
- Treu, T., Auger, M. W., Koopmans, L. V. E., Gavazzi, R., Marshall, P. J., & Bolton, A. S. 2010, *ApJ*, 709, 1195
- Treu, T., & Koopmans, L. V. E. 2004, *ApJ*, 611, 739
- Tu, H., Gavazzi, R., Limousin, M., Cabanac, R., Marshall, P. J., Fort, B., Treu, T., Pello, R., Jullo, E., Kneib, J., & Sygnet, J. 2009, *A&A*, 501, 475
- Vegetti, S., & Koopmans, L. V. E. 2009, *MNRAS*, 392, 945
- Warren, S. J., & Dye, S. 2003, *ApJ*, 590, 673